MASTER THESIS IN MEDICAL PHYSICS AND TECHNOLOGY

Monte Carlo Simulations of Neutron Doses from Pencil Beam Scanning Proton Therapy

Yannick Alexander Broese van Groenou

SUPERVISORS:

Ph.D. Kristian Smeland Ytre-Hauge
Eivind Rørvik

Department of Physics and Technology
June 2017

Abstract

Introduction: Proton therapy is a more advanced form of radiotherapy that allows better dose conformity to the tumor and a homogeneous dose distribution. A side effect however is the production of secondary neutrons generated by the beam particles through nuclear interactions. Neutrons contribute with an unwanted, additional dose, and because neutrons are highly penetrating, they can reach organs and tissue far outside the treatment field. As these particles can have a very strong biological impact, a small dose can lead to a high risk of radiation-induced cancer and other secondary malignancies.

Methods: In this thesis, a cranio-spinal irradiation treatment using intensity-modulated proton therapy for a pediatric medulloblastoma patient was simulated by using the Monte Carlo simulation code FLUKA. Two obliquely opposed proton beams with energies 175 – 190 MeV were used for the cranial fields, and 135 – 150 MeV proton beams for the spinal fields. The therapeutic biological proton dose was 23.4 Gy(RBE). The neutron absorbed dose and ambient dose equivalent were scored for organs at risk and the PTVs. In the treatment, organs at risk were thyroid, liver, colon, stomach, lung, kidneys, bone and bladder. The dose distributions were plotted in a dose-volume histogram, visualized in two-dimensional plots and one-dimensional graphs of dose as a function of depth inside the patient.

Results: The brain was the heaviest exposed organ, receiving a neutron dose of 4 mGy on average. Maximum and minimum doses were 5.7 mGy and 3.1 mGy respectively. The remaining upper organs: eyes, esophagus, trachea and thyroid, all received mean doses around 2 mGy, and maximum doses of 2 -3 mGy, except for the trachea which received 6 mGy. The lower organs: stomach, liver, kidneys, heart and lungs, received maximum doses of 0.3 – 1 mGy. The mean absorbed doses, as well as the equivalent doses were the highest in the brain (236 mSv), and followed by the same upper organs (140-155 mSv). The lower organs received mean dose equivalents of 70 - 80 mSv.

Conclusion: The brain was most heaviest exposed, and received in overall the highest neutron absorbed doses and dose equivalents. The remaining upper organs were less exposed, but the dose distributions are still relatively high compared to the lower organs. The lower organs receive neutron doses, however, they were significantly lower than the organs located in the upper body. The neutron dose decreased from the upper to the lower part of the body. The results obtained in this work could be used as input data in models for risk estimation of radiation induced cancer, and could provide relevant information when different treatment alternatives are to be considered.

Acknowledgements

First of all, I'd like to thank my supervisors Ph.D. Kristian Smeland Ytre-Hauge and Eivind Rørvik.

Thank you Ph.D. Kristian Smeland Ytre-Hauge for giving me this thesis, your very good guidance throughout this entire project and all the help you provided. You gave me the inspiration and motivation to write my thesis and learned me to reflect about my work by giving positive and critical feedback.

Thanks to Eivind Rørvik, for always being there for a conversation whenever I felt the need or to answer my questions. You have backed me up through the entire project whenever I faced a challenge.

I also want to thank Lars Fredrik Fjæra, who provided many good tools to help me process the data that were required for my project. Without your scripts, it would have been quite a challenge to process the data and convert them to correct file formats!

I also want to thank my friend and fellow master student Johan Martin Søbstad, who has always been there to back me up and ready to help with whatever problem I faced in my project. Thank you for helping me to reflect, our conversations, answering my thousands of questions, and for being a great support as a friend. It was extremely social, often almost too social at our working place.

My final thanks goes to my ever-supporting family. A huge thanks to my mom Aleida Knevelman, who supported me all the way and motivated me to continue the work. You were always there when I felt down, and you never lost faith in me, even when I did myself. That was very, very important to me. Thank you, my brother Joel Broese van Groenou, for your never-stopping support. I always enjoyed our conversions, no matter the level of craziness. Our talks and fun we have together always gave me much positive energy. Without you, I would've never figured out what the world's most purposeless fish is and learn this new word poelvocaat. I also thank my dad; Danny Broese van Groenou, my stepmom, Petroesjka Stam, and all four grandparents for their extreme support. You never gave up on me.

Bergen, June 2017
Yannick Alexander Broese van Groenou

Table of Contents

List of Figures

List of Tables

List of Abbreviations

BP	**B**ragg **P**eak
CSDA	**C**ontinuous **S**low **D**own **A**pproximation
CSI	**C**ranio-**S**pinal **I**rradiation
CNS	**C**entral **N**ervous **S**ystem
DICOM	**D**igital **I**maging and **C**ommunications **i**n **M**edicine
DSB	**D**ouble-**S**trand **B**reak
DVH	**D**ose **V**olume **H**istogram
HU	**H**ounsfield **U**nits
HUS	**H**aukeland **U**niversitets**s**ykehus
IAEA	**I**nternational **A**tomic **E**nergy **A**gency
ICRP	**I**nternational **C**ommission on **R**adiological **P**rotection
IMPT	**I**ntensity-**M**odulated **P**roton **T**herapy
LET	**L**inear **E**nergy **T**ransfer
MC	**M**onte **C**arlo
MCS	**M**ultiple **C**oulomb **S**cattering
NCRP	**N**ational **C**ouncil on **R**adation **P**rotection
OAR	**O**rgans **A**t **R**isk
PBS	**P**encil **B**eam **S**canning
PTV	**P**lanning **T**arget **V**olume
RBE	**R**elative **B**iological **E**ffectiveness

SOBP	**S**pread-**O**ut **B**ragg **P**eak
TPS	**T**reatment **P**lanning **S**ystem

1 Introduction

Cancer has existed throughout the entire human history. The oldest record of cancer is written in the Egyptian Edwin Smith Papyrus from about 1600 BC, mentioning breast cancer. The Greek physician Hippocrates referred to cancer as καρκινος, which means crab or crayfish (Hajdu, 2011). According to legend, he gave the name based on the appearance of a solid tumor in which the veins were spreading out from the tumor like the feet of a crab (Sweet, 1981). The English word cancer comes from the translation by the roman encyclopaedist Alus Celsus, of the Greek word καρκινος into Latin: cancer, which also means crab. He recommended surgery for this illness. This proposal has survived for 1000 years (Hajdu, 2011).

From a clinical perspective, cancer is not a disease, but rather a collective term of a large group of diseases. Their properties may vary, such as the age of onset, invasiveness, response to treatment, rate of growth and so forth. Cancer however is characterized by one key property: an abnormal growth of cells due to an imbalance of cell replication and cell death. The expansion of cancerous tissue can result in a tumor. This uncontrolled growth can ultimately evolve into a cell population that invades other tissues and *metastasize* (spread) to other regions in the body. If the cancer cells are invasive and metastasizing, the cancer is considered *malignant.* Malignant tumors are dangerous, ultimately deadly, and difficult to remove (Salt et al., 2004).

Cells in the human body contain DNA. DNA is a vital part of cells as it contains the genetic information for human growth, functioning, cell reproduction, healing of wounds, aging etc. DNA is built as a sequence of genes, formed in long structures known as *chromosomes* (Saha, 2012). When cells multiply, genetic errors in DNA may happen. They occur frequently, and are usually corrected by enzymes. However, some errors may be repaired wrong, resulting in *mutations* that can lead to genetic diseases such as cancer, because information about cell growth is also contained within DNA. Errors and mutations may arise anywhere in the body at any time (Salt et al., 2004).

According to the World Health Organization, cancer is the worldwide leading death cause for people younger than 85 years (Thariat et al., 2013). In 2013, there were a total of 31 651 new cancer incidents in Norway, of which 10 971 people died (Larsen, 2015). The number of cancer incidents rises over time because of the steadily increasing population and life expectancy. Cancer is strongly linked to age (Ruddon, 2007).

Photon therapy is the most common form of radiotherapy. As of today, only a small fraction of patients receive particle therapy. The first person treated with particle therapy was in 1954 at the Lawrence Berkeley Laboratory in California (Amaldi & Kraft, 2005). Since then, more than 150 000 patients have been treated with this therapy. As of 2015, 85% of the patients have received proton therapy and 13% have been treated with carbon ions (Jermann, 2015). Norway received permission for its first proton facility planning by the Minister of Health and Care Services in 2013 (Odland, 2014).

1.1 The History of Radiotherapy

The dawn of radiotherapy started soon after the discovery of X-rays by the German/Dutch mechanical engineer and physicist Wilhelm Conrad Röntgen on November 30th, 1895 (Lederman, 1981; Röntgen, 1898). Only three weeks later, on January 6th, 1896, the first person was treated with X-rays therapeutically by the German second-year medical student Emil Herman Grubbé (Grubbé, 1933). The first patients that were treated in an X-ray facility was in 1896, only a half year after the discovery of the X-rays. They were treated for gastric cancer and basal-cell carcinoma (Lederman, 1981).

From 1913, with the manufacturing of radium and Coolidge tubes, radiotherapy became more standardized. Since then, the aim of radiotherapy has always been to deliver 100% of the dose to the *target volume*, while sparing healthy tissue as much as possible (Lederman, 1981). The awareness of the hazards X-rays can cause started to grow very soon after the discovery of this radiation. In 1915, both the German and British Radiobiological society had already prepared guidelines for physicians in order to avoid unnecessary exposure (Meinhold, 1996).

In the early days of radiotherapy, only low photon energies were achievable. As the research continued rapidly, higher and higher voltage X-ray tubes and linear accelerators were developed. These can provide photons of higher energies, which allows more deep-seated tumors to be treated. Until 1930, the therapeutic dose of X-rays was delivered all in one fraction. It was Henri Coutard, who was the first to propose that the dose could be delivered in several portions spread over time. This is also known as *fractionation* (Schinz, 1930). These, and other developments further improved radiotherapy, which raised the cure rates and lowered the damage to healthy tissue (Thariat et al., 2013).

The first suggestion that also protons and heavier ions could be used as a treatment was made in 1946 by Robert Rathbun Wilson, an American physicist (Wilson, 1946). He argued that protons would scatter less due to the larger mass of the protons compared to photons and electrons. He also stated that the high amount of energy that protons deposit near the end of their range could spare nearby healthy tissues.

1.2 Motivation for Proton Therapy

The difference between particle, photon, and electron radiation therapy lies in the different interaction mechanisms (Bauer et al., 2014; Hong et al., 1996). The dose deposition for photons as a function of depth is characterized by a short build-up region followed by an exponential decrease. This means that also healthy tissue receives a considerable dose, especially for deep-seated tumors, as photons must travel deeper inside the body. Also structures beyond the target volume may receive a significant dose due to the photons' ability of penetration (Yajnik, 2012).

Energy deposition of electrons is characterized by a short build up region, followed rapid decrease afterwards.

Protons have a depth dose curve which is nearly the opposite of that of electrons and photons; they deposit little energy at first, until they nearly reach the end of their range. At that point, they will deposit almost all their remaining energy. Consequently, protons do not penetrate much further after this peak. Therefore, proton therapy enables the ability to maintain a better controlled target volume coverage and better dose conformity, while dose to normal tissue is minimized (Newhauser & Zhang, 2015). Figure 1.1 shows the depth-dose curves of the different particles.

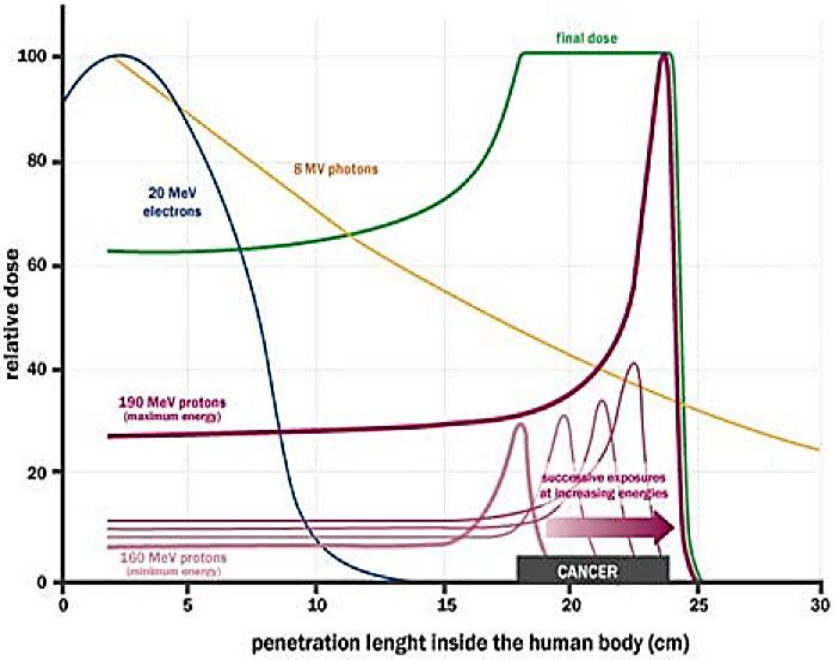

Figure 1.1: A comparison of the depth-dose curves of photons, electrons and protons. Proton therapy is desirable due to the peak of energy deposition. Modified from (INFN, 2008).

1.3 The aim of the thesis

Photon- and particle therapy share the same drawback: the production of neutrons (and other particles) (U. Schneider et al., 2006). Traditional radiotherapy usually requires external beam components to conform and collimate the treatment field. Photons will interact with these collimating and scattering devices and generate neutrons as a byproduct, in addition to the neutrons that are produced within the patient (Engels et al., 1999).

Proton therapy does not necessarily require beam components to improve the dose distribution. Active spot scanning proton therapy only uses external magnets to guide the proton beams and conform the dose to the tumor (Durante & Paganetti, 2016; Kooy & Grassberger, 2015). Abandoning the use of beam modulation devices negates the external neutron production. Unfortunately, the internally produced neutrons cannot be avoided (Brenner et al., 2009).

Even though the neutron dose is negligibly low compared to the total dose, they can still have a strong biological impact; they can hit the vital parts of healthy tissue cells such as DNA, and induce cancer and other second malignancies (Paganetti, 2002; Saha, 2012; U. Schneider & Halg, 2015; Taddei, Krishnan, et al., 2009). Critical organs close to the target volume that should not receive dose, are known as *organs at risk (OAR)*. The *planned target volume (PTV)* is the volume that includes the target, as well as margins to ensure dose delivery to the entire tumor.

Cancer induced by neutrons (or other byproducts) is called *radiation-induced cancer*, or just *secondary cancer*. Secondary cancer is a late biological effect that can occur years after treatment (Roddy & Mueller, 2016). In addition, because neutrons are neutrally charged particles, they have a very strong penetration ability and can reach critical structures further away from the tumor (Newhauser & Zhang, 2015). Neutron radiation has a stronger impact on pediatric patients, because children have a longer life expectancy. Their bodies are still in development, and their organs receive a greater dose on average compared with adults in the same treatment (Zacharatou Jarlskog & Paganetti, 2008).

A study conducted by Schneider et al. in 2002 (U. Schneider et al., 2002), studied the biological impact (fatal malignancies) of neutrons on healthy tissue from two forms of radiotherapy (conventional and intensity modulated) and spot scanning proton therapy, by using a 1 Gy treatment. They showed that the neutron dose is negligible, as the quantities are in the order of 1% of the total dose. Protons also seem to produce more neutrons than in radiotherapy, but due to the much better controlled dose contribution, the proton dose to healthy tissue is so much lower than radiotherapy, that it negates the effect of increased neutron generation. In their study, proton therapy reduced the number of fatal malignancies with almost a factor of 2 compared to photons, demonstrating the effects of proton therapy.

Research about the neutron production in proton therapy did not start until the 1990s. The first study of neutron radiation was conducted by Agosteo et al. in 1998 (Agosteo et al., 1998). It was however first in the 2000s that there were growing concerns about the unwanted neutron production. This concern intensified the research throughout the 2000s (Newhauser & Zhang, 2015). Over time, the research methods improved, especially Monte Carlo simulation of particle therapy. Monte Carlo simulation has always been one of the most important research of proton therapy, but is also used to benchmark experimental measurements. As of today, proton therapy and neutron production remains an active field of research (Newhauser & Zhang, 2015).

In clinics, commercial planning systems do normally not include calculation of neutron dose to the patients. The objectives of this thesis were therefore to-

- simulate an intensity-modulated proton therapy (IMPT) treatment of medulloblastoma in a pediatric patient to score the neutron dose through Monte Carlo simulations, and further
- quantify and visualize the neutron dose distribution in target volumes and organs at risk (OAR).

2 Proton therapy

2.1 Physics of proton therapy

2.1.1 Charged particles interactions

Protons are relatively light ions. Ions interact with matter through three different interactions: ionization and excitation, Coulomb interaction, and nuclear interaction (Newhauser & Zhang, 2015).

Ionization and excitation

In this mechanism, an incident proton collides with an atomic electron. In the collision, energy from the proton to the electron is transferred. If the transferred energy exceeds the binding energy of the electron, the particle is liberated from the atom. This is known as *ionization.* If the transferred energy does not exceed the binding energy, the electron is temporarily *excited* to a higher energy shell, but cannot not escape the atom. In ionization, the kinetic energy of the electron equals the difference in total transferred energy and the electron binding energy (Serway & Jewett, 2013). The radiation of ionized electrons is also called *delta rays.*

Direct ionization is a process in which a particle ionizes an atomic electron directly. It is mainly caused by charged particles (G. Baiocco et al., 2016; Serway & Jewett, 2013).

Indirect ionization is a process in which a particle transfers its energy to a charged particle which in turn ionizes directly. Indirect ionization is mainly caused by particles of neutral charge (G. Baiocco et al., 2016; Serway & Jewett, 2013).

Protons interact in tissue mostly through ionization processes. They lose small quantities of energy per ionization process, but due to the high interaction rate, most of the proton energy is still lost through ionization (Durante & Paganetti, 2016; Leo, 1994).

Coulomb scattering

Coulomb scattering is an interaction in which the proton is heading towards an atomic nucleus instead of one of its electrons. The proton and nucleus both carry a positive charge, so the Coulomb force works repellent. This creates a *Coulomb barrier*. If the Coulomb barrier is too strong, the proton will deflect in its path, i.e. *scatter* from the nucleus (Serway & Jewett, 2013). A proton that scatters not more than a few tens of times in Coulomb scattering is called *plural Coulomb scattering*. A proton that scatters more than that is called *multiple Coulomb scattering (MCS)* (Durante & Paganetti, 2016).

MCS adds an unwanted lateral spread to the proton beam due to the deflections of the protons. Protons have a relatively high grade of deflection in a scatter event because they are very light particles compared to e.g. carbon ions. Heavy ions would therefore add less lateral spread to the ion beam than protons. These ions can be used to increase the precision of the particle beam (Durante & Paganetti, 2016). The scattered protons will deposit their energy somewhat away from the beam axis. Thus, moving away from the beam axis into the lateral spread area, the deposited dose decreases gradually. The region in which this drop in dose occurs is called the *penumbra*. The penumbra can be visualized as a shaded region around the beam axis which represents the dose-fall off of the beam (Gottschalk, 2011).

Nuclear interaction

Nuclear interactions have, for protons, by far the lowest probability of all interaction mechanisms. In the rare cases where the proton can overcome the Coulomb barrier of the nucleus, either because the target nucleus is light and/or a very high kinetic proton energy, the proton gets absorbed by the nucleus and can react with the nucleons (Serway & Jewett, 2013). As a result, the nucleus might eject one or several nucleons. The proton absorption decreases the flux of the therapeutic proton beam gradually (Newhauser & Zhang, 2015).

2.1.2 Stopping power

Ionization and the nuclear interaction are inelastic processes which cause projectile particle to lose its kinetic energy (Newhauser & Zhang, 2015). In proton therapy, they cause the beam particles to slow down. This energy loss is important in proton therapy, as it is strongly linked to dose-deposition. It is called *stopping power*, and is quantified as energy loss per unit *path length*.

If the stopping power is considered in only one dimension, the path length becomes one dimensional. The path is then called *depth* and the stopping power is referred to as **linear** stopping power (Khan & Gibbons, 2014). The stopping power can be considered per interaction type or in its total:

Electronic stopping power only considers the energy loss from ionization processes (Yang et al., 2002).

Total stopping power considers the energy that is lost from all interaction mechanisms, including the nuclear interaction.

The mathematical description of the electronic stopping power is called the *Bethe-Bloch equation*, named after the German physicist Hans Bethe who deduced the expression in 1930 and corrected for relativistic effects in 1932, and Felix Bloch, who corrected the charge z of the projectile particle in the formula (Bethe, 1930; Bloch, 1933). The relativistic version of Bethe-Bloch as given in (Fano, 1963) is:

$$-\frac{dE}{dx} = \frac{4\pi e^4 Z_t Z_p^2}{m_e v^2}\left[\ln\frac{2m_e v^2}{<I>} - ln(1-\beta^2) - \beta^2 - \frac{C}{Z_t} - \frac{\delta}{2}\right] \quad (2.1)$$

Where Z_p and Z_t are the charge of the projectile and target respectively, m_e is the electron mass, e is the electron charge, <I> is the mean ionization potential, β is the particle velocity relative to the speed of light, $\frac{C}{Z_t}$ is the shell correction and $\frac{\delta}{2}$ is the density effect correction.

Plotting the stopping power (dE) vs. depth (dx) gives a *depth-dose curve* (figure 2.2).

2.1.3 Linear energy transfer – LET

Stopping power describes a particle's **energy loss** per unit path length. This energy is not necessarily absorbed, but might instead escape the system. A concept of interest in radiobiology would be a quantification of the energy that is lost by a particle and absorbed by tissue. This quantity is called the *linear energy transfer (LET)* and was first introduced by the American physicist Raymond Elliott Zirkle in 1952 (Zirkle et al., 1952).

LET describes a particle's **energy deposition** per unit path length. Because the dose deposition is very dominated by the ionization mechanism, energy transfer due to ionization only, is also known as the linear *electronic* stopping power (Durante & Paganetti, 2016; ICRU, 2011; Leo, 1994).

Restricted LET only accounts for the energy that is deposited by ionization from primary particles. Ionizing electrons and other second particles that were ionized themselves are excluded in restricted LET (ICRP, 2011).

Unrestricted LET accounts for the energy that is deposited through ionization by all particles, including secondary particles. Therefore, the unrestricted LET is identical to the linear electronic stopping power (ICRP, 2011).

2.1.4 Range

How deep particles can penetrate inside tissue depends on their initial energy and rate of energy loss. The energy loss in turn depends on the number of interactions and how inelastic the interactions are. Consequently, protons will have somewhat different individual ranges, a phenomenon known as *range straggling* (Newhauser & Zhang, 2015).

Therefore, instead of using the path length of an individual proton, it is more relevant to calculate the mean range, the so-called *Continuous Slow Down Approximation (CSDA) range* (Grupen & Shwartz, 2008). The CSDA range is calculated from the stopping power, by integrating the Bethe-Bloch formula over the whole energy range (Grupen & Shwartz, 2008). Figure 2.1 shows the CSDA range for protons in water as a function of energy:

$$R = \int_{E}^{m_o c^2} \frac{dE}{\frac{dE}{dx}} \tag{2.2}$$

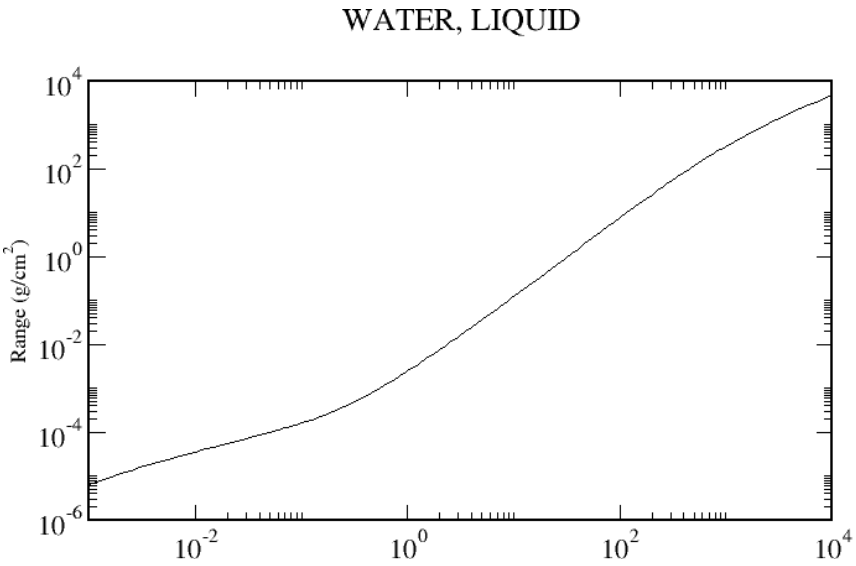

Figure 2.1: the CSDA range of protons in water as a function of energy. Taken from the PSTAR database (NIST US Department of Commerce)

2.1.5 Bragg peak

The depth dose curve, also called *Bragg curve*, following from the Bethe-Bloch equation, shows that ions deposit the largest fraction of their energy towards the end of their range (Paganetti, 2011). This peak is called the *Bragg peak* (BP), first discovered experimentally by the British scientist William Henry Bragg in 1903 for alpha particles (Bragg & Kleeman, 1904).

Figure 2.2 shows the Bragg curve for protons. The overall shape depth-dose curve is very influenced by the ionization process, because the majority of the dose is deposited through this interaction (Durante & Paganetti, 2016). Protons deposit more dose prior to the tumor than heavier ions. The tail distal to the BP is due to slow fragments from nuclear interactions (Jadrnickova et al., 2007).

The BP is the key property in particle therapy; by using ions instead of photons, healthy tissue is more spared prior and adjacent to the tumor. It also allows for better dose conformity and a more homogenous dose distribution to the target volume (Paganetti, 2011).

To cover the extend of a target with particle beams, the beam energy is modulated to obtain a *spread-out Bragg peak (SOBP).* An SOBP is made by adding multiple BPs at different energies together (figure 2.2).

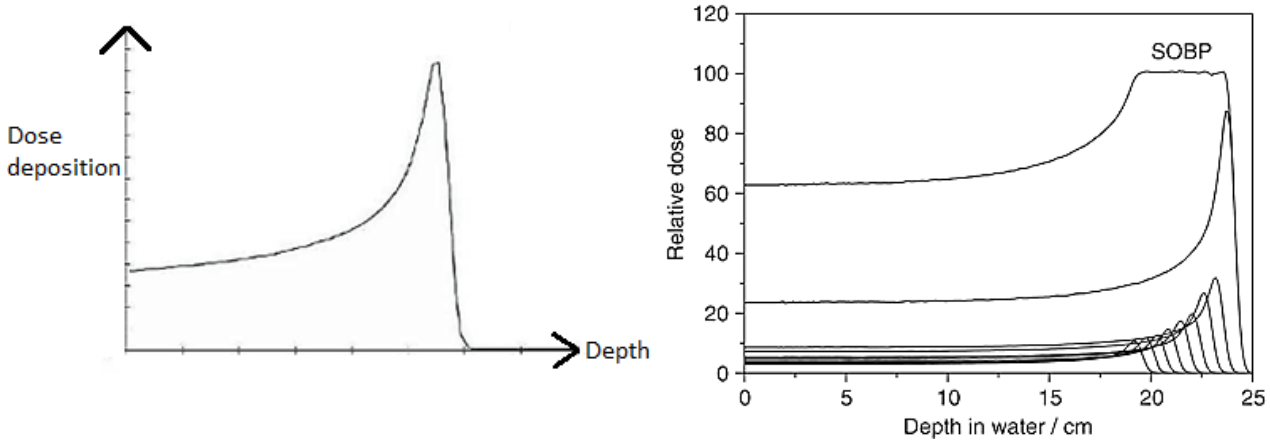

Figure 2.2: Left: Bragg curve for protons. Modified from (Christóvão & Campos, 2010). Right: A combination of multiple BP's create an SOBP which is used to cover the target volume (Stannard et al., 2013).

2.1.6 Beam delivery techniques

To obtain full coverage of the target volume in proton therapy, one can either modulate the initial beam energy, or adjust the beam with passive modulation by using external components:

In **Passive scattering,** as seen in figure 2.3, the shape of the beam is modulated by using flattening devices and scatterers. The beam energy is adjusted by *collimators* (absorbers). This technique is easier to apply, but provides a relatively high risk of side effects after treatment as the beam particles are traveling through matter prior to the patient (Durante & Paganetti, 2016; Zacharatou Jarlskog & Paganetti, 2008).

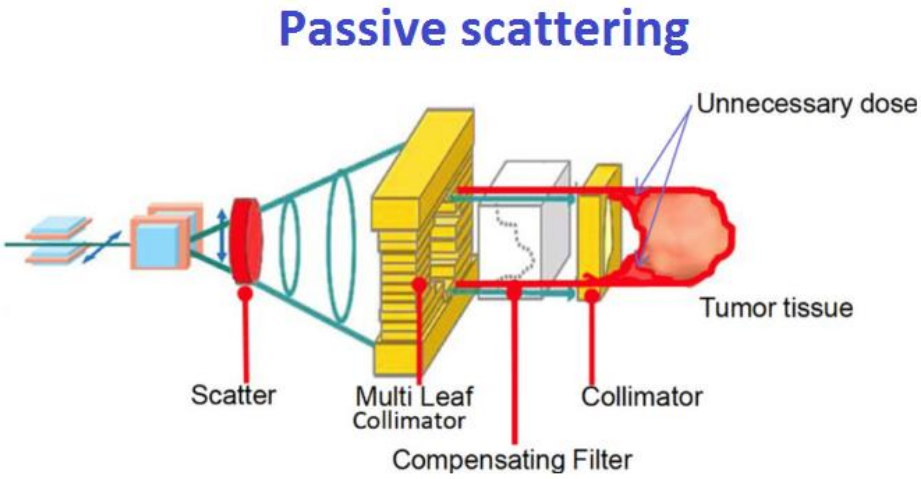

Figure 2.3: Passive scattering modulates the proton beam and conforms it to the target volume by using external modulation devices. Modified from (Durante & Paganetti, 2016).

Active spot scanning, also called *pencil beam scanning (PBS),* is a more advanced delivery technique in proton therapy. The energy of the proton beam is modulated without the need of external modulation devices (figure 2.4). Because the protons are aimed directly at the target volume, this technique is more challenging as more uncertainties such as organ movements are involved. To account for these uncertainties, a higher proton range than strictly required is prescribed so that no part of the target volume can be missed. Active spot scanning provides a very low risk of side effects due to the lack of external modulation elements (Durante & Paganetti, 2016; Zacharatou Jarlskog & Paganetti, 2008).

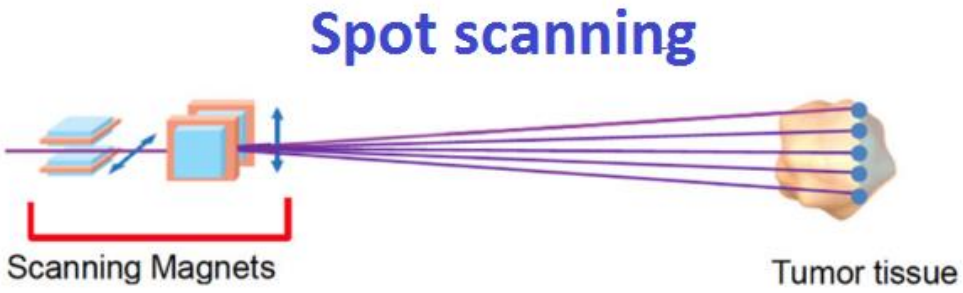

Figure 2.4: Active spot scanning proton therapy only uses magnets to guide the protons to the tumor. Modified from (Durante & Paganetti, 2016)

Intensity modulated proton therapy – IMPT

IMPT uses very narrow proton beans to deliver a dose to every point in the tumor. It allows a very accurately conformed dose to the target, as it can cover all parts of the tumor with the narrow beams. Tumors that are complex-shaped or close to critical organs in the body can also be treated with this technique due to the great precision of IMPT (Khan & Gibbons, 2014; Kooy & Grassberger, 2015)

2.2 Dosimetry and Radiobiology of Proton Therapy

Radiobiology is a field in medical physics that studies the biological effect and impact of ionizing radiation on organisms and living cells. This branch is very important in radiation protection and radiation therapy. The goal of radiation therapy is to kill cancer cells while sparing healthy tissue as much as possible (Hall & Giaccia, 2006). An important concept in radiobiology is *radiosensitivity*. Radiosensitive tissue is easier affected by ionizing radiation than a more radioresistant type (Saha, 2012). Tissues of different radiosensitivity show different effects from radiation in terms of severity which may occur hours to years after treatment (Stokkevåg, 2016).

2.2.1 Dosimetry

Dosimetry is the quantification of radiation exposure, and is used to predict the outcome of a certain exposure to radiation. A large number of dosimetric units and concepts are defined, some based on physical deposition of energy while others aim to quantify biological effects(Cameron, 1991; ICRP, 2007; Khan & Gibbons, 2014).

Absorbed dose

The definition of absorbed dose is the mean energy that is imparted into the medium per unit mass as a result of ionizing radiation. The SI unit of absorbed dose is J/kg (ICRP, 2007).

In clinical applications, the energy from ionizing radiation that is received by tissue per unit mass is referred to as *absorbed dose* or just *dose*. It is used to prescribe the amount of radiation a patient should receive in radiotherapy and quantify the amount radiation from secondary particles, also called *stray radiation*. The unit of absorbed dose used in radiotherapy is Gray: 1 Gy = 1 J / kg (ICRP, 2007).

$$D = \frac{\Delta E}{\Delta m} \tag{2.3}$$

Equivalent dose

The equivalent dose accounts for the damaging properties of the different types of radiation, and can be to quantify the radiation damage that is expected from the absorbed delivered by ionizing radiation. The equivalent dose is obtained by multiplying the absorbed dose with a *radiation weighting factor*. The unit of equivalent dose is Sievert [Sv] (ICRP, 2007)

$$H_T = \sum_R \omega_R D_{T,R} \tag{2.4}$$

where ω_R is the radiation R weighting factor and $D_{T,R}$ is the average absorbed dose in a specific tissue or organ T.

Effective dose

Effective dose is a dose quantity that takes into account both the radiation type as well as the radiosensitivity of the tissue or organ. Weighting the equivalent dose for biological effects, it can be converted into effective dose by multiplying with a *tissue- or organ-specific weighting factor* ω_T (ICRP, 2007):

$$H_E = \sum_T \omega_T H_T \tag{2.5}$$

As of 2007, the International Commission on Radiological Protection (ICRP) defines the following tissue weighting factors (ICRP, 2007):

Table 2.1: Tissue weighting factors defined by the ICRP as of 2007 (ICRP, 2007)

Tissue	ω_T
Brain, salivary glands, bone surface, skin	0.01
Thyroid, Esophagus, liver, bladder	0.04
Red Bone Marrow	0.08
Breasts, stomach	0.12
Gonads	0.13
Lungs	0.16
Colon	0.19
Remainder of the body	0.12

2.2.2 Ambient dose equivalent

Effective dose and equivalent dose are non-measurable quantities as they are defined in the body of the individual. The International Community of Radiation Units and Measurements (ICRU) has defined the ambient dose equivalent. This is a measurable quantity meant for practical use. Such a unit is called an *operational dose quantity* (ICRU, 1993).

The definition of the ambient dose equivalent (and all other operational dose quantities) for area monitoring are based on a phantom, which is the ICRU sphere. This sphere has a diameter of 30 cm, and is made of tissue-like material. It approximates the human body with regard to attenuation and scattering of radiation (Wernli, 2004). It is calculated from the particle fluence, for example neutrons, by using conversion coefficients (Howell et al., 2016).

The ambient dose equivalent, H*(d), with d = 10 mm (H*(10), is used for area monitoring of penetrating radiation (ICRU, 1993). As visualized in figure 2.5, it is the dose equivalent that would be deposited by radiation in the ICRU sphere at a depth of d = 10 mm. The unit of ambient dose equivalent is Sievert (Sv) (Wernli, 2004). The H*(10) is not organ or tissue-specific (Howell et al., 2016). However, in most cases, the H*(10) gives a considerable estimate of the effective dose a patient would receive (Wernli, 2004).

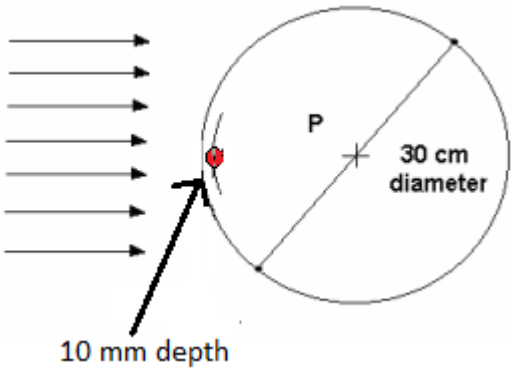

Figure 2.5: Visualization of the geometrical definition for measurement of the ambient dose equivalent (H(10)) for strongly penetrating radiation. Modified from (Bedogni, 2006)*

2.2.3 Relative biological effectiveness – RBE

The relative biological effectiveness (RBE) translates the dose of one radiation quality into another that induces the **same biological effect**. The reference radiation quality is normally either photons of 250 keV or photons from Co-60 ions, depending on the considerable clinical data and experience available. (Beyzadeoglu et al., 2010; Khan & Gibbons, 2014). Mathematically, the RBE is the ratio between the absorbed dose of a test radiation and the absorbed dose of reference radiation in which both doses induce the same biological effect (Khan & Gibbons, 2014):

$$RBE = \frac{absorbed\ dose\ of\ test\ radiation}{absorbed\ dose\ of\ reference\ radiation} \tag{2.6}$$

The RBE is endpoint-specific. An *endpoint* is a specific biological effect, e.g. cell killing, or DNA damage. Therefore, different RBE's exist for different biological effects (Khan & Gibbons, 2014).

The RBE is important when prescribing and planning the treatment. If the RBE of radiation is estimated too high, the delivered dose will be too low for proper tumor control. An underestimated RBE would give a too high dose to the tumor, which potentially can result in more complications after treatment. RBE is found to depend on dose, particle type, energy, cell type, track structure, LET, and endpoint (Ballarini et al., 2013; Grassberger et al., 2011; Jones, 2015b).

The RBE and its uncertainties are found to increase as one goes further away from the treatment field. Thus, organs and tissue receiving low doses may have a less certain RBE (Stokkevag et

al., 2014). In addition, there is still a lack of biological input parameters which limits the predictability of biological effectiveness (Grassberger et al., 2011).

While the RBE is known to vary, protons have a standard numeric RBE = 1.1. This is an average value determined from in vitro experiments when proton therapy was still young. This constant however neglects all RBE dependencies such as dose, endpoint or proton beam properties (Grassberger et al., 2011; Paganetti, 2014).

By multiplying the RBE of a particle with the physical dose it delivered, one gets the *biological dose* (ICRU, 2007):

$$Biological\ dose\ [Gy(RBE)] = D[Gy] * RBE \tag{2.7}$$

2.2.4 LET vs RBE

LET is one of the quantities thought to be strongly linked to the RBE and is therefore an important quantity in radiobiology for protons (Jones, 2015a, 2015b; Manem et al., 2015). Figure 2.6 shows a typical RBE-LET relationship for protons. Prior to the turnover point, RBE is proportional with LET. It means that the higher LET, the more biological effective the radiation is. After the maximum point, with increasing LET, the RBE decreases due to an overkill by radiation. Overkill has a negative impact on the biological effectiveness of the radiation (Grassberger & Paganetti, 2011).

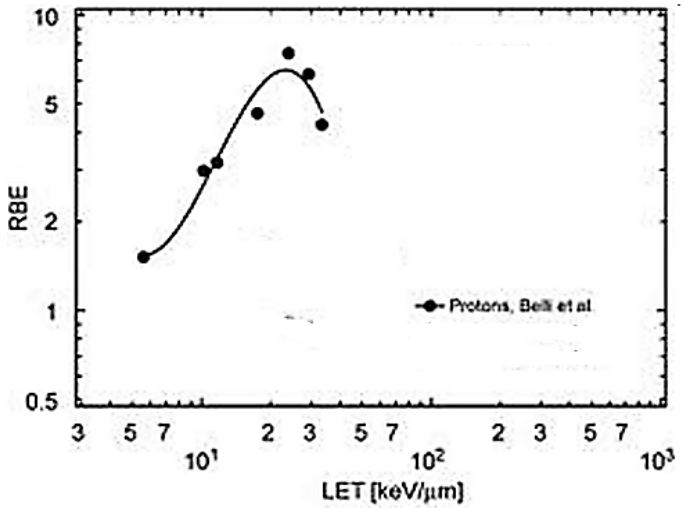

Figure 2.6: A RBE-LET relationship for protons found from cell irradiation experiments. Modified from (Villagrasa et al., 2014).

3 Neutrons in Proton Therapy

When protons are absorbed by nuclei in a nuclear interaction, other particles can be ejected from the nucleus as a result. These emitted particles are called *secondary particles*, or just *secondaries*. In water, the most common particles produced by incident protons are secondary protons, neutrons, deuterons, tritons, α-particles and He-3 (Paganetti, 2002). Figure 3.1 illustrates the nuclear interaction mechanism.

Secondaries add a relatively low, but unwanted additional dose to the patient during proton therapy. Dependent on the mass, energy and charge of the secondary, they may have a strong biological impact on the patient. The biological effectivity is higher for slow and heavy particles. (Durante & Paganetti, 2016; U. Schneider & Halg, 2015).

Neutrons are of particular concern in proton therapy because they have no net charge, and are one of the greatest contributors to the secondary dose with a typical share of 1% of the total dose before the BP (U. Schneider et al., 2002). They usually have a high RBE which is heavily energy-dependent, and can easily penetrate healthy tissue beyond the treatment field as they are not subject to the Coulomb force (Durante & Paganetti, 2016; Newhauser & Zhang, 2015). These particles are believed to have a high capability of inducing second malignancies such as induced cancer, carcinogenesis, DNA lesions and mutation, cell inactivation and cell killing (Engels et al., 1999; Newhauser & Zhang, 2015). Neutrons are further responsible for enhancing the penumbra of proton beams as they tend to increase both the longitudinal and lateral range of the therapeutic beam (Durante & Paganetti, 2016).

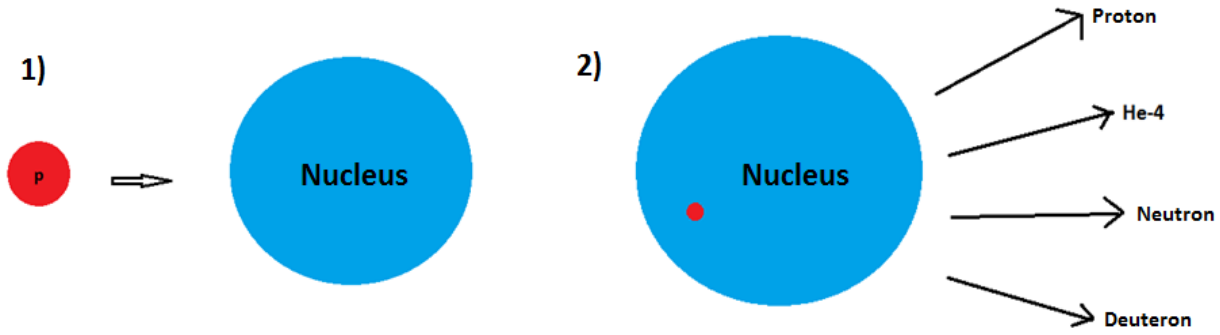

Figure 3.1: Illustration of the nuclear interaction. In step 1), the proton overcomes the Coulomb barrier and is absorbed by the nucleus. In step 2), the nucleus emits one or more particles due to the instability caused by the absorbed proton

3.1 Neutron production

3.1.1 Cross section and production frequency

The neutron production depends on the nuclear interaction cross section of the proton beam. A *cross section* is the projected mutual two-dimensional area of an incident particle and the target, and resembles the probability of a specific interaction. Both particles must meet within the cross section area to interact. The higher the interaction cross section, the higher chance the interaction occurs (Beiser, 2002) The cross-section SI unit is m^2, but in physical applications, the unit barn is used ($1b = 10^{-28}m^2$) (Henley, 2007).

The nuclear interaction cross section of protons is inversely proportional to their energy, but also depends on the subatomic properties of the materials in the beam path such as the atomic number (Durante & Paganetti, 2016). Because the Coulomb force between the incident proton and target nucleus is repellant, the proton must reach a certain minimum energy before a nuclear interaction can occur, meaning that the cross section for this interaction should be zero when the proton's energy is below this threshold. This implies that neutron generation also requires a minimum energy, this is demonstrated in figure 3.2.

Figure 3.2 shows the cross section of protons incident on O-16 (as in water) for neutron production in nuclear interactions as a function of the proton energy. The peak is at ~11 MeV. Although the cross section decreases with increasing proton energy after the peak, protons can still generate neutrons at energies over 200 MeV. These data indicate that protons of energies

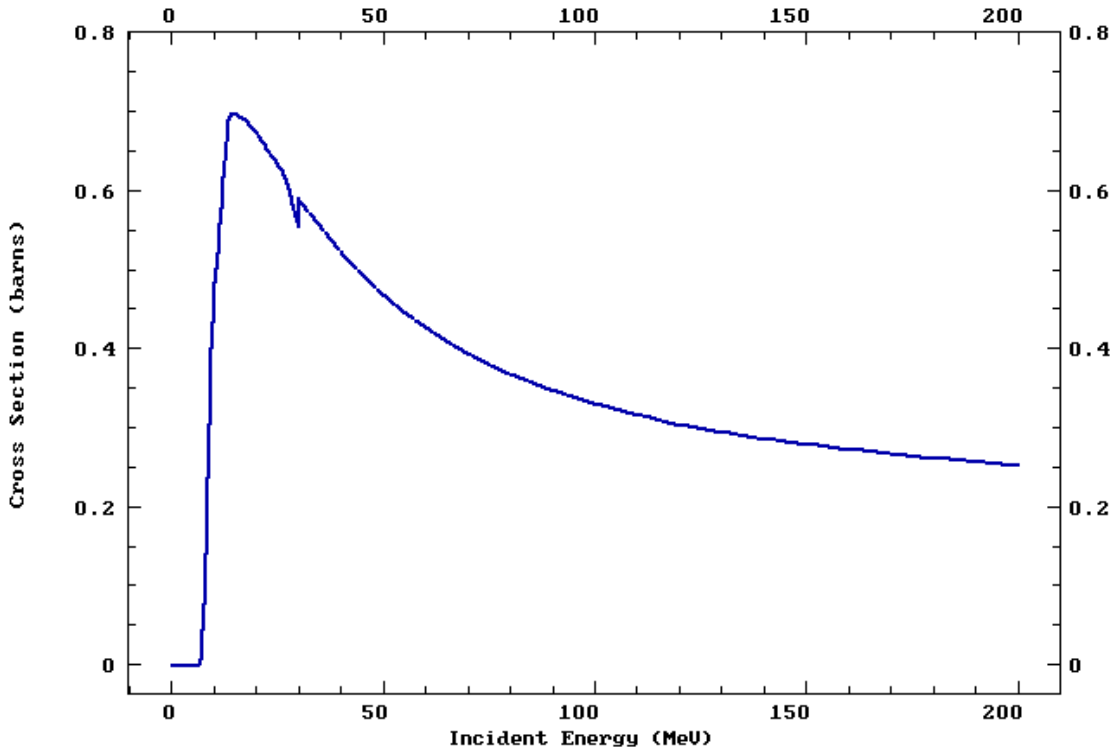

Figure 3.2: The cross section for neutron production by protons incident on O-16 as a function of proton energy. Data retrieved from online library TENDL-2014, datasheets from (Koning & Rochman, 2012).

below approximately ~ 7 MeV are not able to create neutrons in O-16. According to a study performed by Paganetti et al. in 2002, they found that on average 0.63 neutrons were produced per primary proton (160 MeV) in water (Paganetti, 2002).

3.1.2 Neutron contribution components

Assuming protons have energies above the neutron production threshold, neutron generation is unavoidable when protons travel through matter. In proton therapy, the production of these secondaries can have two components:

External neutrons are created outside the patient. They are only an issue in passive scattering because of the modulation components in the beam path prior to the patient. Protons interact with these structures, and generate neutrons and other secondaries as a result. This is also known as *radiation leakage* (U. Schneider & Halg, 2015). Studies on external neutron doses conclude that the treatment head is the main source. The dose contribution depends on the geometry and aperture of the treatment head as well as the facility (Brenner et al., 2009; Jiang et al., 2005; Zheng et al., 2011).

Internal neutrons are created within the patient (Zacharatou Jarlskog et al., 2008). They are an issue in both active and passive proton therapy as protons must travel through the patient to reach the tumor. Therefore, the internal component cannot be prevented (Islam et al., 2017). This contribution can be greater for proton therapy than photon therapy, and might in some cases negate the advantage of protons over photons, although the quantification of risk from neutrons includes considerable uncertainties (Paganetti, 2011; Zacharatou Jarlskog & Paganetti, 2008).

Several studies have demonstrated this advantage of proton beam scanning over passive scattering. They conclude that scanning indeed provides an overall lower secondary dose distribution and thus, a lower expected induced risk of second malignancies (Jiang et al., 2005; U. Schneider et al., 2002). In figure 3.3, we see a comparison of internally produced neutron

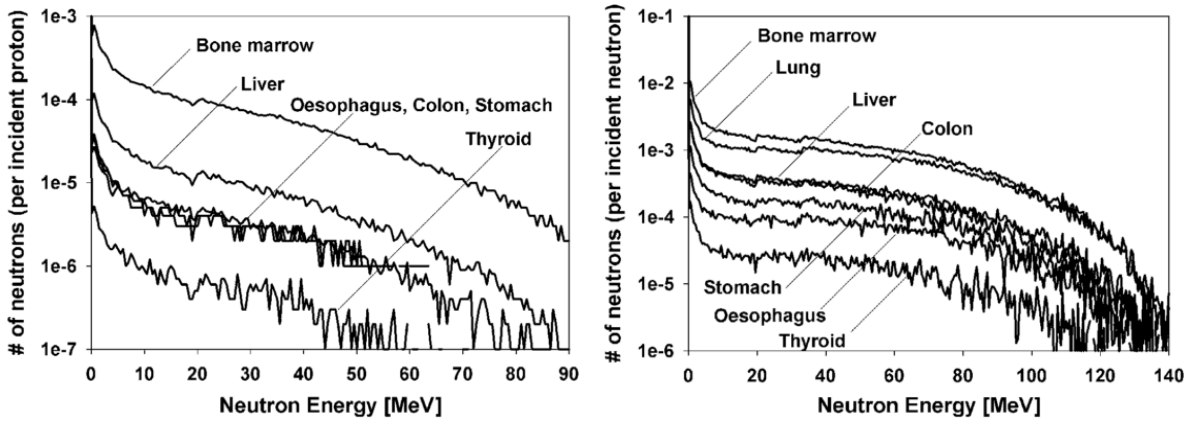

Figure 3.3: A simulation study that compared the neutron yield generated outside and inside a patient with lung cancer. Left: Internal neutrons. Right: external neutrons. Notice how externally produced neutrons have in general a higher energy, and a yield which is ~10 times that of internal neutrons (Jiang et al., 2005).

and external neutron yields as a function of proton energy, as studied by Jiang et al. in 2005 (Jiang et al., 2005).

3.2 Neutron characteristics

The key properties of neutrons are energy, and the strongly energy-dependent RBE. Neutrons are not quantified by LET because they do not ionize directly due to their lack of charge (Paganetti, 2013).

3.2.1 Energy

The energy spectrum of neutrons generated by protons spans 10 orders of magnitude (Newhauser & Zhang, 2015).

Because energy is a key property of neutrons, they are classified after their energies. The following neutron classification comes from the National Counsil on Radation Protection (NCRP) (NCRP, 1971), but classifications may vary:

- Thermal neutrons: $E < 1$ eV
- Intermediate neutrons: 1 eV $< E < 10$ keV
- Fast neutrons $E > 10$ keV

A Monte Carlo simulation study conducted by Sengbusch et al. in 2009 quantified the neutron energy spectrum generated by unmodulated proton beams of different energies incident on a water phantom (Sengbusch et al., 2009).

A result from their study is shown in figure 3.4. It describes the neutron yield and energy that was produced per proton at different beam energies. They showed that both the neutron production and energy increases with increasing proton beam energy. As seen from figure 3.4, their study indicated that protons can generate neutrons with energies from a few eV (thermal neutrons) up to nearly the initial proton energy (fast neutrons) (Sengbusch et al., 2009).

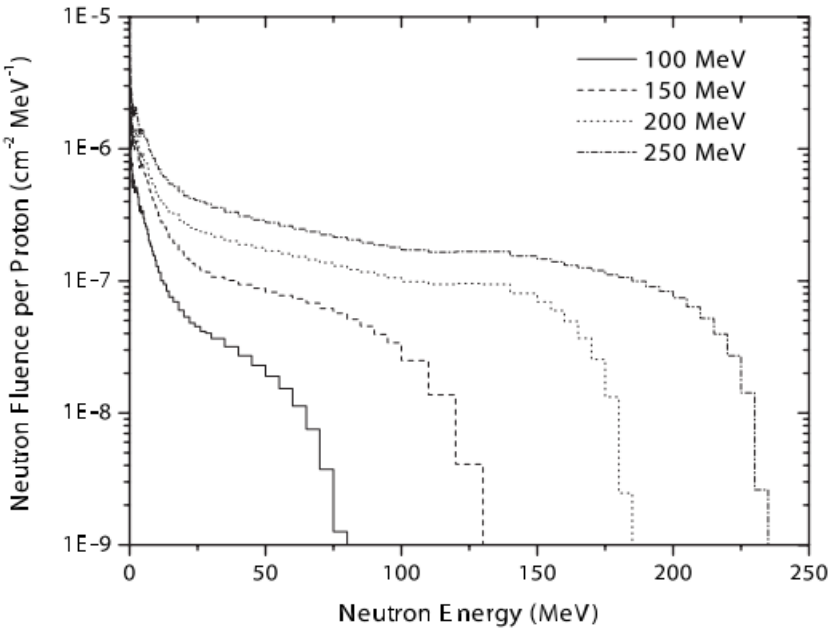

Figure 3.4: Neutron yield as a function of neutron energy, produced by unmodulated proton beams of different energies incident on a water phantom (Sengbusch et al., 2009).

3.2.2 RBE

There is a strong indication that the neutron RBE for second cancer induction is greater than for cell killing. (Engels et al., 1999). This emphasizes the threat neutrons impose with regard to cancer induction and possibly other second malignancies.

A simulation study from 2016 by Baiocco et al. investigated the neutron RBE for the endpoint DNA double-strand break (DSB) cluster lesions as a function of energy (G. Baiocco et al., 2016). Their result showed that the peak of the neutron RBE is around 1 MeV, see figure 3.5. As seen from the figure, neutrons of only 0.1 MeV can already have an RBE $\sim$10 which is about 10 times higher than the standard proton RBE of 1.1.

The first peak in figure 3.5 resembles the maximum neutron effectiveness for DSB clusters. The second peak is due to fast neutrons; they are able to create more complex DSB clusters. These clusters are more challenging for cells to repair, and thus, are more likely to fail (G. Baiocco et al., 2016).

Generally, the neutron RBE as a function of energy tends to behave as a normal distribution: the RBE increases until a maximum point after which it decreases again. This is also shown in figure 3.5. Another study of Baiocco et al. concluded that the neutron RBE tends to be maximum at energies around 1 MeV (G Baiocco et al., 2015).

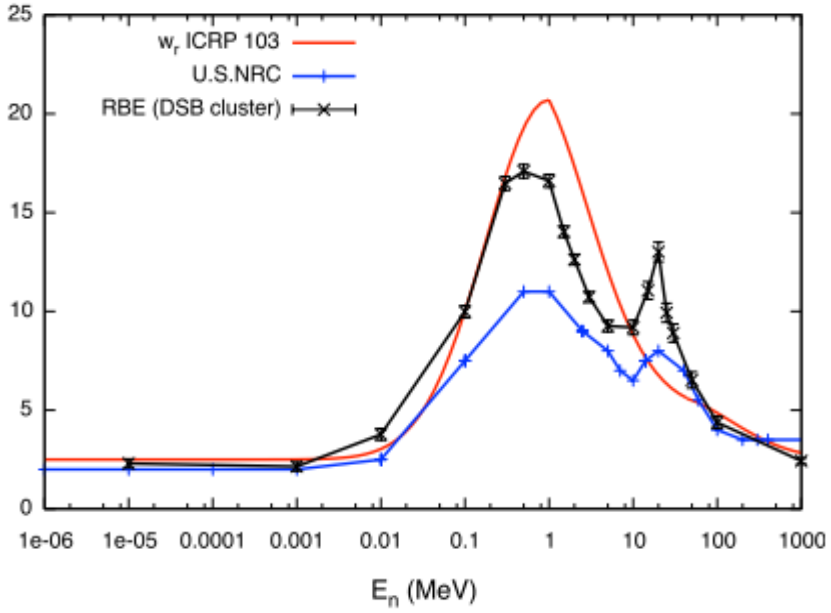

Figure 3.5: Neutron RBE for DSB cluster lesions as a function of energy. (G. Baiocco et al., 2016). The RBE was compared with the neutron radiation weighting factors from ICRP.

3.2.3 Neutron radiation weighting factor

Radiation weighting factors are an estimate of an higher biological effectiveness of radiation, applied in radiation protection. These factors are used to convert absorbed dose into equivalent dose (ICRU, 2007).

Because the biological effectiveness of neutrons is strongly energy-dependent, it is the only type of radiation of which the weighting factor is a continuous function of energy instead of a fixed number. As of 2007, the International Committee of Radiation Protection (ICRP) defines the following neutron radiation weighting factors where E is the neutron energy (ICRP, 2007)

$$\omega_R = \begin{cases} 2.5 + 18.2e^{-\frac{[\ln(E)]^2}{6}}, & E < 1\ MeV \\ 5.0 + 17.0e^{-\frac{[\ln(2E)]^2}{6}}, & 1\ MeV < E < 50\ MeV \\ 2.5 + 3.25e^{-\frac{[\ln(0.04E)]^2}{6}}, & E > 50\ MeV \end{cases} \quad (3.1)$$

3.3 Neutron interactions

Neutrons have no net charge, and therefore not subject to the Coulomb force when travelling through matter. They only interact and change direction when they actually hit a nucleus in their path.

Neutron interaction cross sections mainly depend on the type of target nucleus and neutron energy. The cross section is heavily energy-dependent and inversely proportional to the particle's energy. The *mean free path* is proportional to the energy, implying it is inversely proportional to the neutron cross section. The mean free path is the distance a particle travels between two interactions (Rinard, 1991). Fast neutrons are therefore expected to have stronger penetration abilities than their slow counterparts.

3.3.1 Neutron capture

In neutron capture, the neutron is absorbed by the target nucleus and will not be reemitted, but will emit other particles instead. Neutron capture occurs only at low energy levels. The cross section is inversely proportional to the neutron energy (Park & Kang, 2011). Only two neutron capture reactions are relevant in proton therapy: $^{14}N(n,p)\,^{14}C$ and $p(n,\gamma)d$ (Paganetti, 2002).

In the $p(n,\gamma)d$ reaction, the result is recoiling deuterons and photon emission. The photons have each an energy of 2.2 MV, which is sufficient for ionizing electrons. These delta rays and recoiling deuterons will deliver a dose to the target (G. Baiocco et al., 2016). The cross section for this interaction was found by Gerald M. Hale and Hartmut M. Hofmann in 2004 and compared with other data (Hale & Hofmann, 2004). Their result, shown in figure 3.6, indicates that the neutron capture cross section decreases significantly with increasing neutron energy.

The other possible, but less likely interaction is a neutron being captured by nitrogen: $^{14}N(n,p)\,^{14}C$, where the resulting nucleus and proton have an energy of 0.04 MeV and 0.58 MeV respectively (G. Baiocco et al., 2016). A disadvantage with this interaction is *neutron activation*: the neutron creates the radioactive iosotope ^{14}C. This exposed the patient to radioactive radiation.

Neutron capture is mostly dominated by thermal neutrons (Park & Kang, 2011).

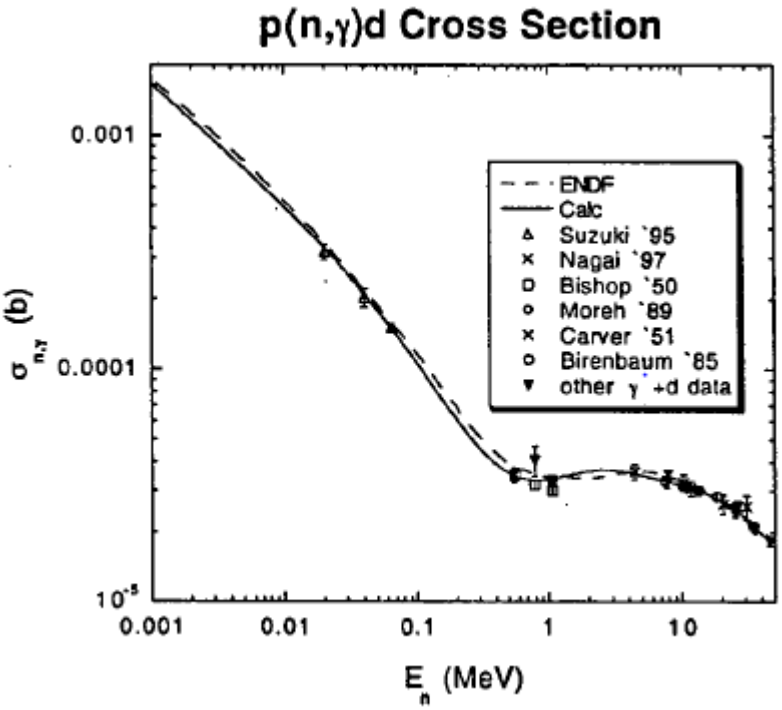

Figure 3.6: The probability of this interaction is inversely proportional to the neutron energy except at 1 MeV (Hale & Hofmann, 2004).

3.3.2 Elastic scattering

Elastic scattering is an interaction in which a neutron collides with a target nucleus and the total kinetic energy is conserved. Thus, kinetic energy may be transferred to the target, but will not excite the nucleus. The amount of energy the neutron transmits to the target depends on the direction of motion of the projectile, and is further closely linked to the target's mass. When the neutron collides with the target, it may either rebound completely or bounce off in a different reaction. If the neutron rebounds completely, the kinetic energy of the neutron is conserved. Otherwise, the nucleus receives kinetic energy from the neutron and will recoil. The recoiling target will lose its energy through ionization (Park & Kang, 2011).

Elastic scattering is mostly dominated by intermediate neutrons (Park & Kang, 2011).

3.3.3 Inelastic scattering

Inelastic scattering is a reaction in which a neutron collides with a target nucleus and is absorbed. This causes the ejection of neutrons and possibly other secondary particles from the nucleus. Energy from the neutron absorption excites the nucleus into a temporarily higher energy state. The nucleus will de-excite by emitting photons (Park & Kang, 2011; Serway & Jewett, 2013).

Inelastic scattering will not occur if excitation of the target requires more energy than the neutron possesses. The energy required for excitation depends on the mass of the target nucleus. (Park & Kang, 2011)

Inelastic scattering is mostly dominated by fast neutrons (Park & Kang, 2011).

3.4 Neutron dose distributions

In 2008, Jarlskog et al. demonstrated two neutron dose scoring methods with simulation. The first method is to assign a weighting factor to every single dose deposition dependent on the particle type and energy. The other method is averaging the total dose over all particles, applying a single neutron weighting factor, and scaling the equivalent dose after the neutron fluence. They concluded that the first method is the most accurate, but also most time consuming. This demonstrates the trade-off in simulation: accuracy vs computation time (Jarlskog & Paganetti, 2008).

The neutron dose can be quantified either as a separate contribution in addition to the therapeutic dose, or as part of the total dose in which the primary and secondary dose are combined (U. Schneider & Halg, 2015). The neutron dose is most commonly expressed in terms of neutron dose equivalent per primary dose: H/D, but can also be regarded per primary particle (Wang et al., 2010).

The dose distribution can be distinguished between *in-* and *out-field (U. Schneider & Halg, 2015)*:

In-field dose refers to the dose delivered by primaries and secondaries within the planned treatment field.

Out-field dose is delivered to areas outside the treatment volume. It is mainly caused by scattered particles and deep penetrating neutrons.

The neutron dose cannot be measured directly since these particles are indirectly ionizing (Paganetti, 2013). Instead, the dose deposition of the charged particles emerging from the neutron nuclear interactions must be scored.

3.4.1 Dependencies

The delivered neutron biological dose depends on biological factors such as tissue type, distance from the target volume, type of organ, individual patient parameters such as age, and field parameters involving the treatment field size and target volume. Studies have found that the neutron dose is inversely proportional to the distance from the target (Zacharatou Jarlskog et al., 2008; Zacharatou Jarlskog & Paganetti, 2008).

The secondary dose is proportional with field size because a greater proton fluence is required for a bigger treatment field (Jarlskog & Paganetti, 2008). Treatment of deep-seated tumors requires high proton beam energies which also increases the neutron production, as well as their energies (Zacharatou Jarlskog et al., 2008).

3.4.2 Risks and uncertainties

Many studies have been conducted to measure the secondary dose and risk estimation. The neutron dose is typically in the order of 10^{-3} Gy per treatment Gy for spot scanning (Islam et al., 2017; U. Schneider et al., 2002). This dose is negligibly small, but because of the high neutron RBE, the neutrons still increase the risk of second cancer considerably. Neutron dose and risk estimations are most important for young and pediatric patients as their body is in full development and due to their long life expectancy (Roddy & Mueller, 2016; Zheng et al., 2008).

Neutron dose quantification as well as secondary risk still follow with considerable uncertainties due to limited literature and experimental data available. (Jarlskog & Paganetti, 2008; Stokkevag et al., 2014; Zacharatou Jarlskog et al., 2008). Generally, the uncertainty of RBE is proportional with decreasing dose, implying that doses delivered further away from the treatment field also have an increased uncertainty in RBE, including the estimation of neutron biological dose (Stokkevag et al., 2014).

4 Monte Carlo Simulations

A *Monte Carlo simulation (MC)* is an algorithmic generation process of random numbers. It is used to model complex processes and systems that depend on stochastic variables, which are represented by random numbers. Monte Carlo can be used to conduct random experiments many times and observe the results. This allows a good understanding of the probability and statistics of the experiments. It is therefore a powerful tool as it can provide a reliable insight of the behavior of stochastic processes, and can help to improve and develop theories that are based on statistical knowledge (Kroese et al., 2014).

The three most common uses of Monte Carlo simulation are sampling, where information about different outcomes of stochastic experiments or models are observed, estimation of numerical outcomes from experiments or models to study possible correlations and behavior, and optimization, in which randomness is used to optimize complex models to get a more accurate outcome by reducing the "noise" (Kroese et al., 2014).

Monte Carlo simulation is applied in many branches and fields, e.g. industrial engineering, physics, economics and statistics.

4.1 Monte Carlo Simulation in Proton Therapy

Monte Carlo simulations are considered the gold standard for dose calculations in particle therapy. They provide high accuracy, because they can track all particles in the simulation, and use theoretical and experimental data to apply the physics of interactions to every single particle at every step. The accuracy also increases due to the wide range of different types of tissue and other media that can be simulated in Monte Carlo (Paganetti et al., 2008).

The accuracy of Monte Carlo simulations depends on the number of histories (i.e. particles) N. The statistical uncertainty decreases with $1/\sqrt{N}$. This shows a trade-off between accuracy and simulation time: getting higher precision requires more particles which in turn increases the computation time (Das & Paganetti, 2015).

Uncertainties of Monte Carlo simulations can emerge from the tracking of particles. At every step, a particle can interact with matter dependent on the cross section distribution of the interaction. This uncertainty is proportional to the number of steps (Das & Paganetti, 2015).

Clinics use commercial *treatment planning systems (TPS)* to perform calculations for radiation plans on patients. TPS usually rely on pencil beam algorithms instead of MC to reduce computation time while at the same time obtaining reasonable accuracy. PB can, despite their reasonable accuracy, have problems with dose calculations at low dose levels, very heterogeneous tissue, etc (Bauer et al., 2014; Catli & Tanir, 2013; Jiang & Paganetti, 2004; Juste et al., 2010; Paganetti et al., 2008; Tourovsky et al., 2005).

4.2 The FLUKA Monte Carlo Code

FLUKA is an integrated multipurpose Monte Carlo code for the simulation of particle interactions and transport. It allows the study of 60 different particles. Hadrons can be simulated up to 20 TeV, neutrons and muons at any energy, electrons and photons at energies ranging from 1 keV to several thousand TeV. FLUKA is capable of tracking particles in electric and magnetic fields, and simulate both polarized and optical photons (A. Ferrari; Ferrari et al., 2014; T.T. Böhlen, 2014)

FLUKA, which has a library of microscopic models, enforces conservation laws at every single reaction step and reaction type when possible to ensure consistency. The results are compared and benchmarked to experimental data at single interaction levels. This can result in predictions with a minimal set of free parameters, and consequently, in complex cases and scaling properties and scaling laws, arising naturally from the underlying physical models, which provides predictivity where experimental data is not found (A. Ferrari; Ferrari et al., 2014; T.T. Böhlen, 2014).

FLUKA is supported by a graphical interface called Flair (A. Ferrari; Ferrari et al., 2014; T.T. Böhlen, 2014).

4.2.1 FLUKA Input

User input data is read by FLUKA from an input file written in ASCII format. The input consists of different commands specified through standard FLUKA *cards*. These cards offer a broad variety of options for scoring most qualities of possible interest, so users are not required to write their own code. The input file is typically structured in the following manner (A. Ferrari; Ferrari et al., 2014; T.T. Böhlen, 2014):

- Titles and comments for documentation purposes.
- Description of the problem geometry.
- Definition of the materials.
- Material assignments.
- Definition of the particle source.
- Definition of the requested detectors to score physical quantities e.g. dose, fluence or energy.
- Definition of biasing schemes.
- Definition of problem settings such as transport cuts, energy cut-offs, step size, physical effects not simulated by default, etc.

- Initialization of the random number sequence.
- Number of requested histories.

For simulation settings that are too complex to be handled by regular input cards, the user can implement user routines provided by FLUKA or write their own. FLUKA and the routines are written in Fortran 77 (A. Ferrari; Ferrari et al., 2014; T.T. Böhlen, 2014) . In this thesis, one user routine: Source, is used.

4.2.2 CT images in FLUKA

FLUKA enables the user to import CT images to create complex geometries such as a patient body.

CT images and Hounsfield units

CT imaging uses x-rays to penetrate the patient's body and registers the absorption of this radiation. The absorption is expressed in terms of a linear absorption coefficient μ. CT images are a result of the absorption coefficient distribution acquired from these scans. Darker regions in the image indicate less absorption than brighter regions. CT images are able to achieve tissue density information (Smith & Webb, 2010).

In order to compare images from different CT scanners easily, the English engineer Godfrey Hounsfield introduced the *Hounsfield units (HU)*, also known as *CT numbers*. The Hounsfield unit scale expresses the tissue linear absorption coefficient acquired from CT relative to the linear absorption coefficient of water (Smith & Webb, 2010):

$$HU = \frac{\mu_{tissue} - \mu_{water}}{\mu_{water}} \tag{4.1}$$

Hounsfield further defined the HU (water) $\equiv 0$, $HU(bone) \equiv 1000$ and $HU(air) \equiv -1000$.

In proton therapy, HU's are directly related to the stopping power relative to water and can be used to translate CT numbers into tissue density (Smith & Webb, 2010).

Calibration Curve

A calibration curve is the relationship between HU and material density or stopping power. Stopping powers can be acquired by using a simplified Bethe-Bloch equation. The relationship is usually acquired by calibrating the CT scanner where materials with known elemental composition are used as a phantom (Schaffner & Pedroni, 1998).

In FLUKA, the calibration curve comes from the work of Schneider et al. who established a new method to convert CT numbers into mass density, and calculated the CT numbers for 71 human tissues. Their work provided HU from 1024 to 1600 (W. Schneider et al., 2000). Six years later, the HU range was further extended to 3070 by the work of Parodi et al in 2006 (Parodi et al., 2007).

When CT images are imported into FLUKA, the program can translation the CT numbers into tissue material. Since every CT voxel is designated a HU, FLUKA assigns a material to every voxel. The result is saved by the program in a file called material file, which contains the information about the tissue material composition of the geometry.

4.2.3 Digital Imaging and Communications in Medicine - DICOM

The DICOM format is a standard that can store, handle, print and transmit information in medical imaging. A DICOM file contains all the required information about the radiotherapy on patients. Information includes the patient's anatomy, coordinates of regions of interest, gantry angles, beam input parameters etc. DICOM files are used to make the import/export of medical data between equipment and software easier, since there are many different manufacturers of medical equipment which use different standards (Fjæra, 2016).

Four DICOM files used in this project were: CT image, RT Structure set, RT Plan and RT dose.

CT image

The information of CT images is stored in terms of HU units. The CT images form a long sequence of files where every image corresponds to a separate planar slice in the z-direction of the DICOM coordinate system.

RT Structure Set

The RT Structure Set contains information about delineation of volumes, regions of interest, and structures such as OARs and their coordinates. This information can be used to analyze the dose deposition in target volumes and OARs.

RT Plan

The RT plan file contains information about the treatment plan delivery; beam parameters, dose prescription, eventual beam modification components, patient position etc.

RT Dose

The RT dose file contains the calculated dose distribution from TPS. There are usually several RT dose files; one for each treatment field and one for all fields combined.

5 Methods and Materials

The objective of the thesis was to recalculate neutron doses for a cranio-spinal irradiation treatment for a pediatric medulloblastoma patient using intensity-modulated proton therapy by using the Monte Carlo code FLUKA.

Cranio-spinal irradiation (CSI) is a cancer treatment for the central nervous system (CSN) where the whole spine and brain are irradiated (Stokkevag et al., 2014). It is one of the most technically challenging treatments because of the very large and complex-shaped target volume. The target volumes usually overlap, or are close to, several critical organs. Irradiation of critical organs may cause severe post treatment effects such as cardiac disease and radiation-induced cancer, which should be avoided (Packer et al., 2013).

The most common CNS tumor treated with CSI in pediatric patients is medulloblastoma (Brodin et al., 2011). Medulloblastoma is a fast growing tumor in the cerebellum of the brain, which controls important motoric functions such as balance, speech and posture. This malignancy accounts for 2% of all tumors that start in the brain, but still accounts for 18% of all pediatric brain tumors. Over 70% of pediatric medulloblastoma incidents occur under the age of 10 (ABTA, 2006).

The neutron absorbed dose and dose equivalent were scored and evaluated for the spinal and cranial PTV, as well as several organs: brain, eyes, heart, kidneys, liver, lungs, stomach, thyroid trachea and esophagus.

5.1 Treatment planning of the CSI patient

The treatment plan was provided by Camilla Stokkevåg (Stokkevag et al., 2014). It was calculated in the Eclipse treatment planning system at Haukeland Universitetssykehus. Four treatment fields were applied: two spinal fields, and two obliquely opposed cranial fields. The proton beam energy was 175 – 190 MeV for the cranial fields, and 135 – 150 MeV for the spinal fields. The patient was put in prone position. The therapeutic dose was 21.27 Gy, which converts to a biological proton dose of 23.4 Gy(RBE). The aim of the treatment was to cover the target volume with 95% of the prescribed dose. Organs at risk in the treatment were esophagus, thyroid, liver, colon, stomach, lung, kidneys, bone and bladder.

5.2 Preparing the Monte Carlo simulation

Because the treatment plan consisted of four treatment fields, each field was simulated separately. To set up the simulation in FLUKA, information from the DICOM files about the treatment plan were imported into the program. Required information were beam input parameters and configuration, as well as CT images of the patient.

5.2.1 Importing DICOM files into FLUKA

The RT plan from the TPS was required to create the beam input data such as beam energy, angles, and configuration. Because FLUKA, as of version 2.2-3, cannot import DICOM files other than CT images directly, these data were extracted from the RT plan and rewritten in a FLUKA input file format. For this purpose, Lars Fredrik Fjæra had created a tool that translates data from TPS to FLUKA (Fjæra, 2016).

To save computation time, the regions outside the patient in the CT images were set to vacuum. This was also done by the tool of Fjæra, and the resulting images were imported into the Monte Carlo code. Based on these images, FLUKA created a voxelized patient geometry, and stored the information in a new input file. This voxel file was imported into FLUKA.

FLUKA also converted the CT numbers of the images into material (tissue), assigning each voxel a type of tissue material. The result was stored in another input file and imported into FLUKA.

5.2.2 Further preparation of the simulation in FLUKA

Scoring

Two quantities were scored: neutron dose and neutron ambient dose equivalent. This dose equivalent weighting factor in FLUKA was based on the ambient dose equivalent weighting factors provided by the ICRP and the work of Pelliconi (A. Ferrari; T.T. Böhlen, 2014).

Beam configuration

The standard beam input card in FLUKA allows the user to create a Gaussian-or flat-shaped mono-energetic beams. The Source user routine enabled the implementation of complex-shaped and energy-modulated beams to create SOBPs. The source file was imported into FLUKA.

For each field, a range shifter was applied. This was simulated as a slab of water with a thickness of 5.7 cm. By using a range shifter, a smaller energy variation in the proton beam is required to create the SOBP.

Improving statistics

Neutron dose quantities are very small in proton therapy. Therefore, the statistics need to be improved. This was performed by enhancing the neutron production through *biasing* by shortening the mean free path of all particles by a factor of 50.

Optimizing computation time

To save simulation time, all particles that cannot produce neutrons were cut. Particles are unable to produce neutrons when their energies are below the neutron production threshold. Therefore, particles with energy under this threshold were cut. A possible energy cut-off for the most time-consuming and abundant particles were considered: protons, electrons and photons.

To find the neutron production energy thresholds, the neutron-production cross-section as a function of energy for protons, electrons and photons were considered. Because the human body consists 99% of hydrogen, carbon, nitrogen and oxygen, the neutron production cross-sections were evaluated for these elements.

This information was found in the online "Evaluated Nuclear Data File" database. This database, provided by the International Atomic Energy Agency (IAEA), contains reviewed experimental and theoretical data from most types of inelastic interaction cross-sections, for most particles, in most elements. It followed that protons could not be cut in energy, but electrons and photons could as their neutron production energy threshold was found to be 6 MeV.

5.3 Processing of the data

After the simulations had run, the obtained data was processed by another script created by Fjæra. It calculated the dose deposited in every voxel in the patient geometry, normalized the data, performed dose calculations, and wrote the output in a single DICOM file.

5.3.1 Structuring The Data

The FLUKA scoring results were stored as dose files. Dose files were created per field. The script of Fjæra read in the dose files and the RT struct DICOM file, to calculate the doses each structure received.

5.3.2 Normalization of the data

Normalization is used to scale data properly. The proton doses in FLUKA must be scaled after the delivered proton dose calculated in the TPS in order to obtain correct dose distributions according to the treatment plan from the TPS. Neutron doses were scaled with the same normalization factors as the proton doses since neutrons were produced by the protons.

Unfortunately, the number of primary particles used in the treatment plan in the TPS was unknown. Therefore, normalization by using the number of primary protons was not possible.

Instead, geometrical normalization was applied. In geometrical normalization, the 1000 closest voxels surrounding the *isocenter* (center position) of the target volume in both the TPS and FLUKA were taken. It was assumed that the median dose in this area was approximately 100%

in FLUKA, and in the TPS. The FLUKA dose distribution was normalized after the ratio of the FLUKA mean dose and TPS mean dose. Clearly, the geometrical normalization method is less accurate, but also gives acceptable results.

For every field, one normalization factor was obtained and applied in Fjæra's script so that the dose files were correctly normalized to their corresponding fields.

5.3.3 Data Process Calculations

After normalizing the neutron doses, the FLUKA units of GeV/g were converted to Gy by multiplying the neutron dose with a factor of $1.602176462 * 10^{-7}$. Because neutron doses usualy are given in the order of mGy in dose considerations, the units were further converted to mGy. The unit of dose equivalent in FLUKA given in pSv, was converted to mSv.

Combining all fields

After the data was processed, the total dose was obtained by combining all fields.

The output result was written in DICOM format. The data processing was done for the absorbed dose and dose equivalent separately. This resulted ultimately in two DICOM files: one containing the absorbed dose, the other containing the dose equivalent. Finally, proton dose files were provided by Johan Martin Søbstad for the comparison of neutron doses with proton doses and directly converted to DICOM format. The proton dose files also contained stray radiation doses, and thus actually represent the total dose. However, the additional doses are negligibly small.

5.4 Obtaining The Results

The doses were evaluated by calculating a DVH and obtaining the DVH metrics $D_{98}, D_{80}, D_{50}, D_{20}, D_2$. In addition, the neutron dose distributions were considered by two-dimensional plots, and evaluated by plotting one-dimensional graphs of dose vs. depth.

The three DICOM dosefiles were used to obtain all results. The following results were obtained:

5.4.1 Dose Volume Histogram – DVH

A dose-volume histogram summarizes the three-dimensional dose distribution as absorbed in the structure volume, by quantifying how the dose was distributed volumetrically within the structure. It shows the total amount of volume the dose depositions occupied in the given organ or PTV.

The two neutron DICOM dosefiles were processed in Slicer, version 4.6.2. Slicer is a program for medical research purposes that can analyze, process, and provide three-dimensional visualizations of medical images.

An extension of the program, SlicerRT (Pinter et al., 2012), imported the biological structures from the RT structure file and the DICOM dose files, and computed a DVH for every volume available. Slicer is also capable of plotting the DVH graphically. It can however, only plot one volume at a time. Therefore, the output data was exported instead, and a tool was created by the author to plot the DVH of several volumes simultaneously. All DVHs in this thesis are cumulative DVH plots.

Because a DVH summarizes the three-dimensional dose distribution in a two-dimensional plot, all spatial information is lost. Therefore, a DVH cannot tell how the dose was exactly distributed within the given structures. To obtain spatial information, two-dimensional plots were created.

From the DVH, Slicer provided dose values for the structures. These values are the minimum doses that were received by a given percentage of the volume of the organs. For example, D_{98} is the minimum dose that was received by 98% of the given volume. The metrics obtained from the DVH were: D_{98} , D_{50}, D_2 and the mean dose. D_2 and D_{98} represent the "statistical maximum and minimum dose" respectively. D_{50}, the minimum dose that 50% of the structure received, is also called the *median dose*. The dose values were obtained for both the absorbed and dose equivalent.

5.4.2 2D plot

To obtain spatial information about the neutron doses and to compare with the therapeutic proton doses, the dose distributions were visualized in 2D plots by drawing them upon the CT images of the patient. The CT images show the patient in the transverse plane. OARs were delineated in the figures to show their exposure to the neutron radiation. Four CT images, spread over the patient body were chosen; one slice of the head, one at the neck, one at the thorax and one at the diaphragm. 2D plotting was enabled by another script written by Fjæra.

5.4.3 1D plot

By choosing a small volume that extends a few cm in the coronal and sagittal plane, but covered the whole body in the transverse plane, the actual neutron dose deposition vs depth could be graphed. The volume extensions in the patient were chosen such that the volume covered most of the PTV in the sagittal plane with sufficient extensions of a few cm in the coronal plane.

The one-dimensional plots show the actual dose deposition as a function of depth in the patient, along the therapeutic beam line. A graph was obtained for every 2D plot. A script for 1D plotting was provided by Johan Martin Søbstad.

6 Results

6.1 Neutron Dose Distributions

Figure 6.1 shows the dose distribution of neutron absorbed dose (a), total dose (b), and neutron dose equivalent in one section of the patient. From plot b, we see that the proton/total dose decreases rapidly when moving away from the PTV (indicated in red). Neutron absorbed doses were observed in the entire body of the patient. Thus, all organs appearing in the slices were exposed to secondary neutrons produced by the primary protons or in the range shifters. Further dose plot comparisons are found in Appendix C.

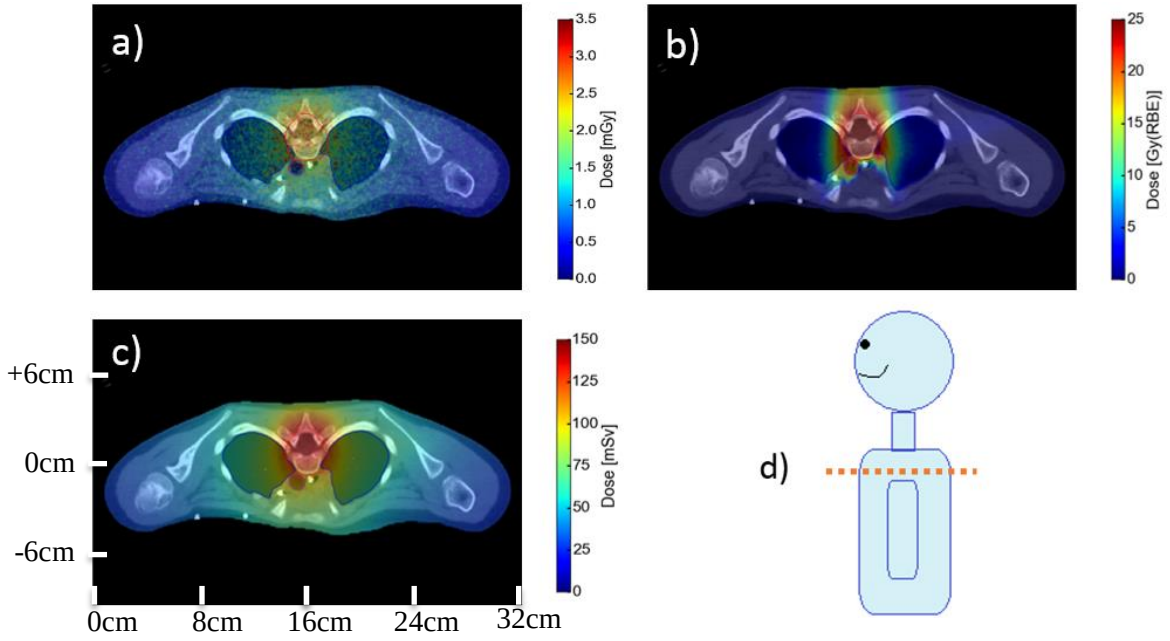

Figure 6.1: The neutron dose distribution compared with the proton dose distribution. a) absorbed neutron dose, b) proton dose, c) neutron dose equivalent. d) indicates the location of the slice in the patient body.

Figure 6.2 visualizes the neutron absorbed dose distribution two-dimensionally in slices at four heights in the patient. The arms in figure 6.2 d) do not show dose distributions because due to the dose calculation process, vacuum was set outside the patient body RT structure (which excluded the arms) as described in section 5.2.1.

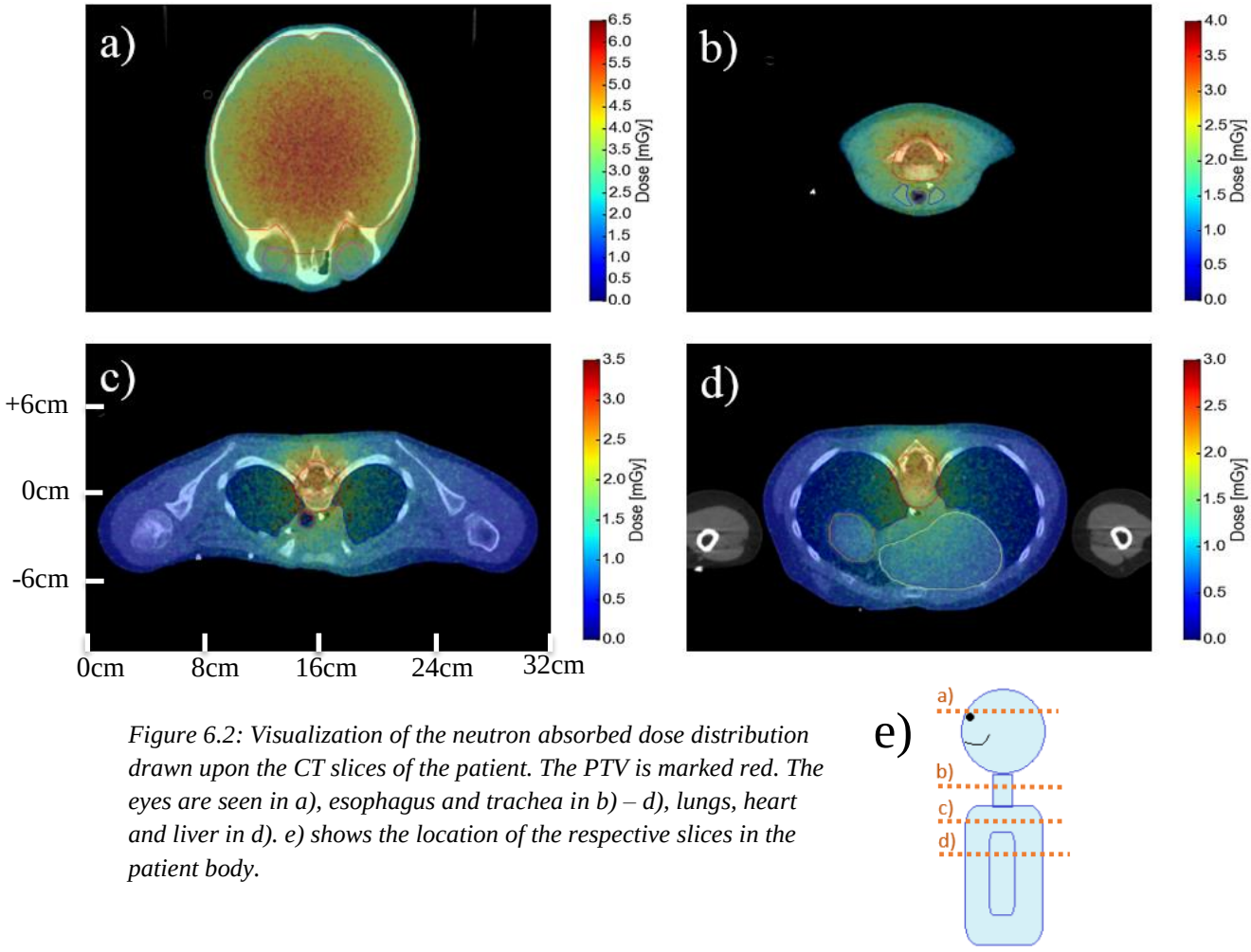

Figure 6.2: Visualization of the neutron absorbed dose distribution drawn upon the CT slices of the patient. The PTV is marked red. The eyes are seen in a), esophagus and trachea in b) – d), lungs, heart and liver in d). e) shows the location of the respective slices in the patient body.

As seen from the 2D plots, neutron doses are observed throughout the entire patient body. The highest concentration of neutron doses were found within and adjacent to the PTV, and decrease gradually as one moves away from the PTV. The exposure was the highest in the upper part of the body (head + neck); 2 – 6 mGy. The lower parts (thorax and diaphragm) received doses between 0.5 – 3 mGy.

The eyes, esophagus, trachea and brain were most exposed during the treatment. Lungs (blue), liver (orange) and heart (yellow) as seen in figure 6.2 d) were also exposed, but to a less degree than the upper organs.

The neutron dose equivalent in figure 6.3 seemed to be proportional to the neutron absorbed dose distribution, as the dose equivalent was distributed similarly; the center of highest dose concentration within the PTV, and decreased away from the PTV:

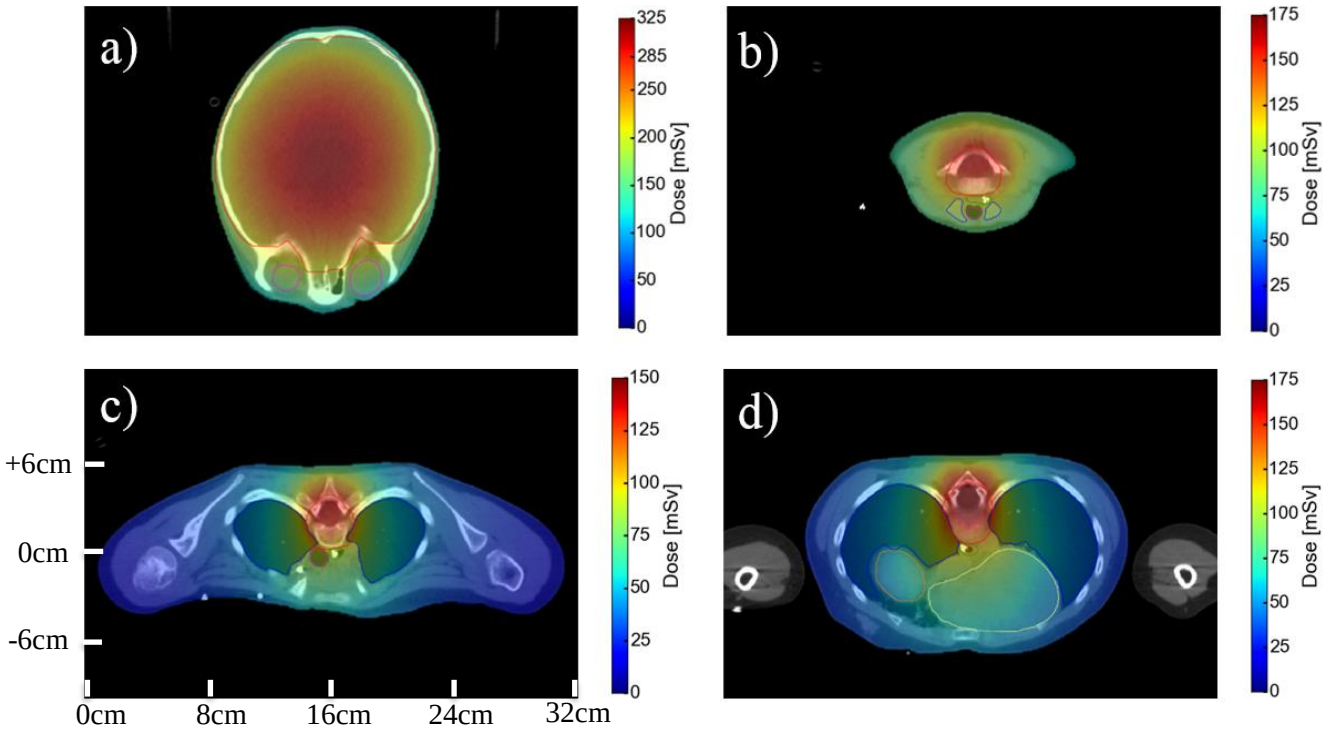

Figure 6.3: Visualization of the neutron dose equivalent distribution drawn upon the Ct slices of the patient. The PTV is marked red. The eyes are seen in a), esophagus and trachea in b) – d), lungs, heart and liver in d). e) shows the location of the respective slices in the body of the patient.

The same upper organs: brain, eyes, trachea and esophagus also receive the highest dose equivalents compared with the lower structures in the lower parts of the body.

To get an idea of how the neutron dose exactly was distributed as a function of depth in the patient, figures 6.4 and 6.5 show one-dimensional plots of the neutron absorbed dose and dose equivalent distribution respectively.

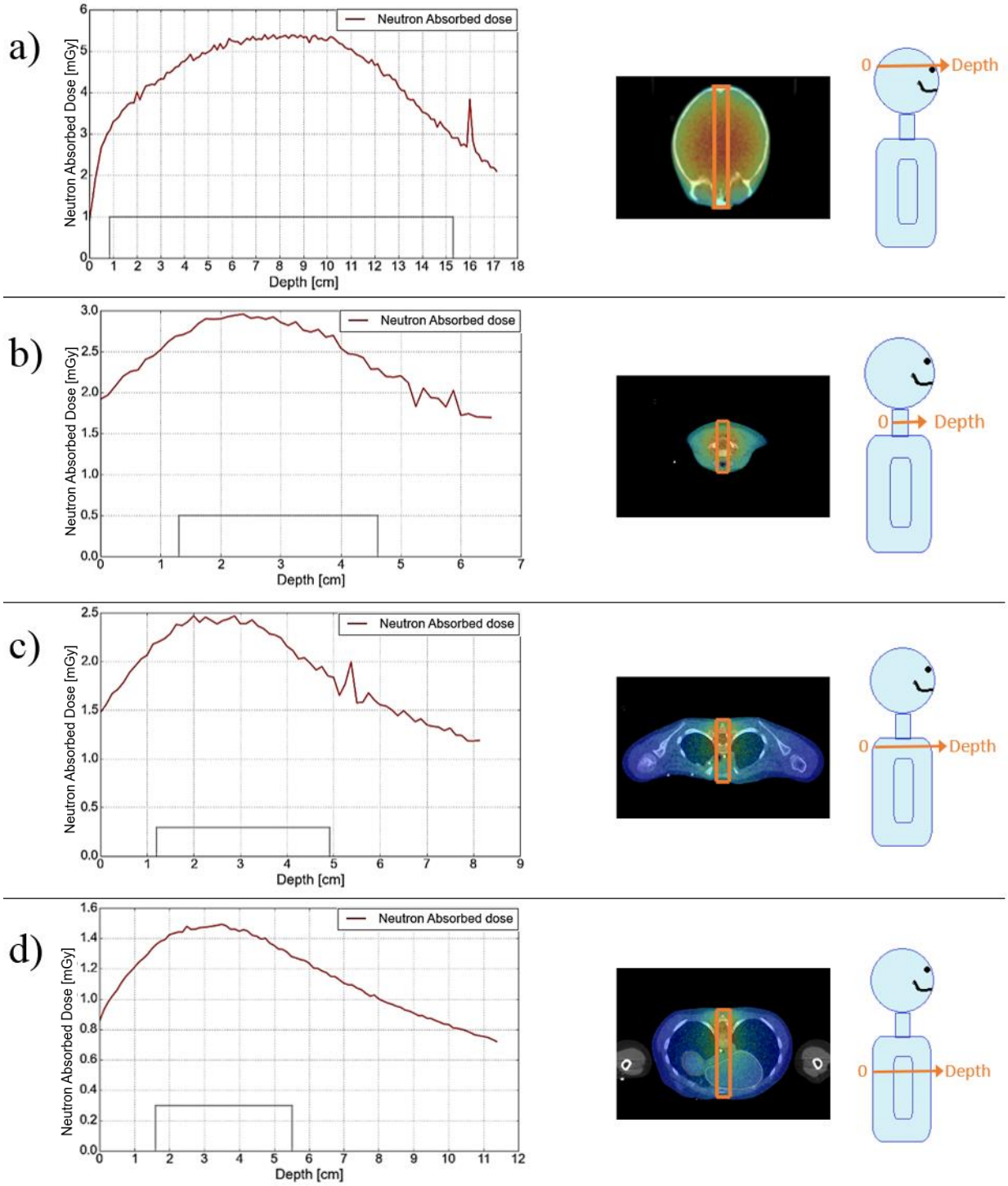

Figure 6.4: The neutron dose as a function of depth in the patient. The 1D plots are shown on the left sides. The gray box under the graphs indicate the PTV at the actual depth inside the patient. The figures in the middle indicate the part of the 2D plot that was graphed, with an orange box. On the right, the location in the patient at which the 1D graphs were taken are indicated, as well as the definition of depth in the patient

The neutron dose was relatively low at the skin of the patient and increased until it reached a maximum around the middle of the PTV, as shown in figure 6.4. Maximum doses were approximately 5.3 mGy, 3 mGy, 2.5 mGy and 1.5 mGy in figures 6.6 a), b), c) and d) respectively. The decrease rate of the neutron dose after the maximum was lower than the rate of increase in the neutron doses.

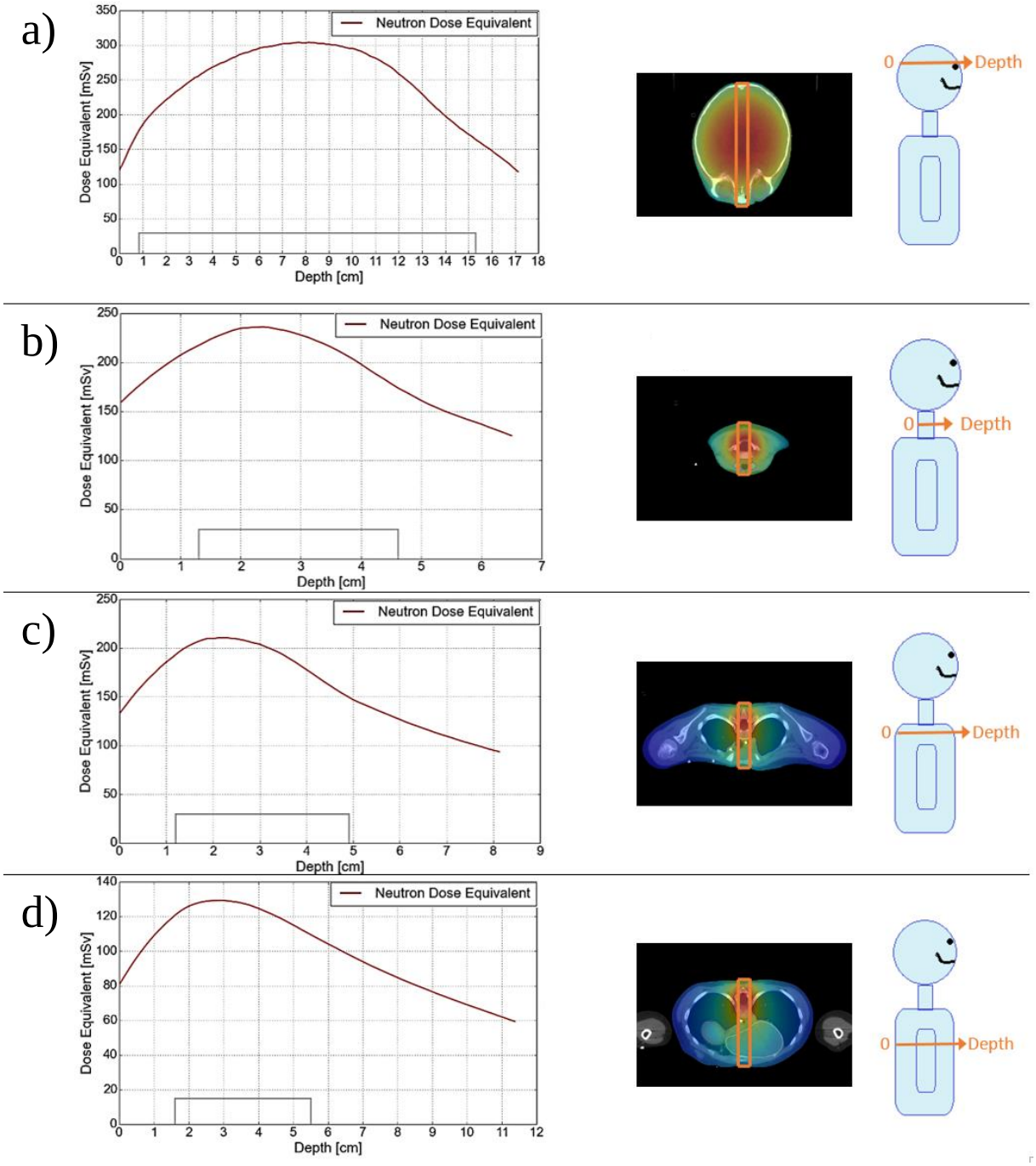

Figure 6.5: The neutron dose equivalent as a function of depth in the patient.

In the graphs in figure 6.4 a) and c), a peak was observed, occurring right after the PTV and the SOBP where protons fully stopped. These peaks correspond to a sudden increase in

neutron dose of ca. 0.5 mGy. Figure 6.4 b) does showed signs of a peak, although it was not at the same magnitude as in figure 6.4 a) and c). No peak was observed in figure 6.5 d).

The neutron equivalent 1D graphs show the same behavior; a build-up region until a maximum point is reached, which was located in the PTV. Maximum points in figures 6.5 a), b), c) and d) were ~300 mSv, 230 mSv, 210 mSv and 130 mSv respectively. The decrease rate is lower than the rate of increase. No peak was observed in the one-dimensional graph.

6.2 Neutron Doses in Organs

The organ-specific neutron doses were quantified by using the DVH and DVH metrics. A selection of organs is shown in figure 6.6. The DVHs and corresponding DVH metrics for all organs are found in Appendix A and B respectively.

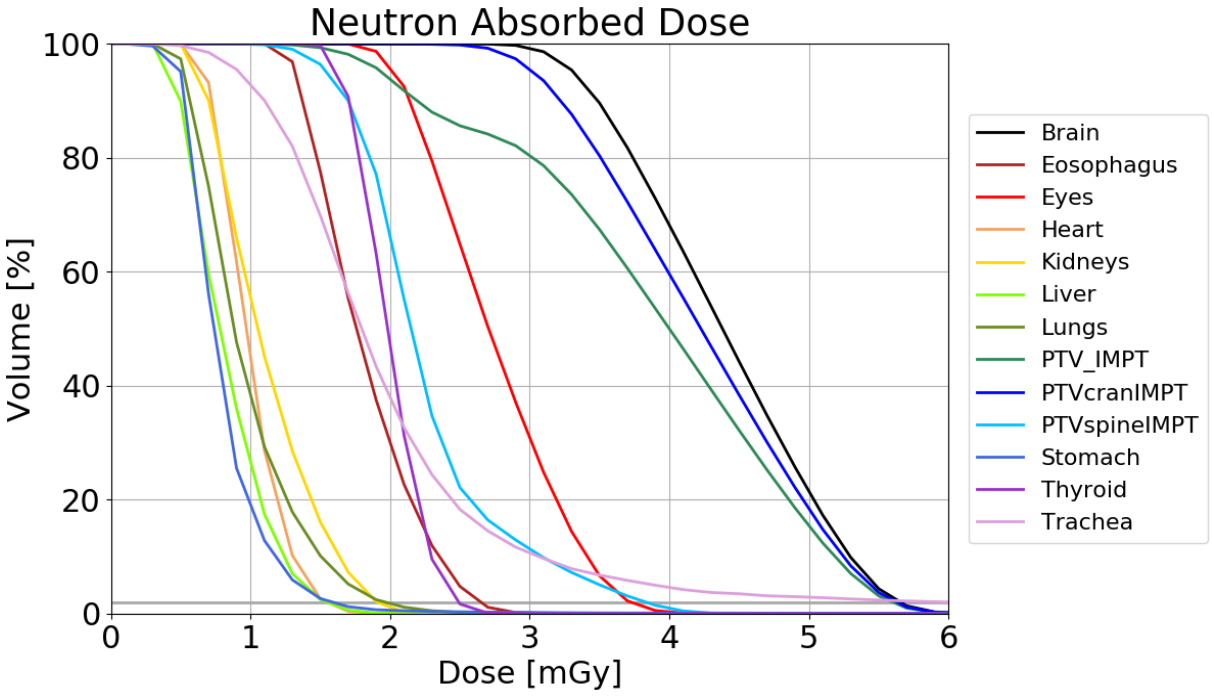

Figure 6.6: Absorbed dose DVH for all organs. The lower organs lower in the patient body absorbed less neutron dose than the upper organs. The grey line indicates the volume at 2% and represents the level of D_2, the maximum dose.

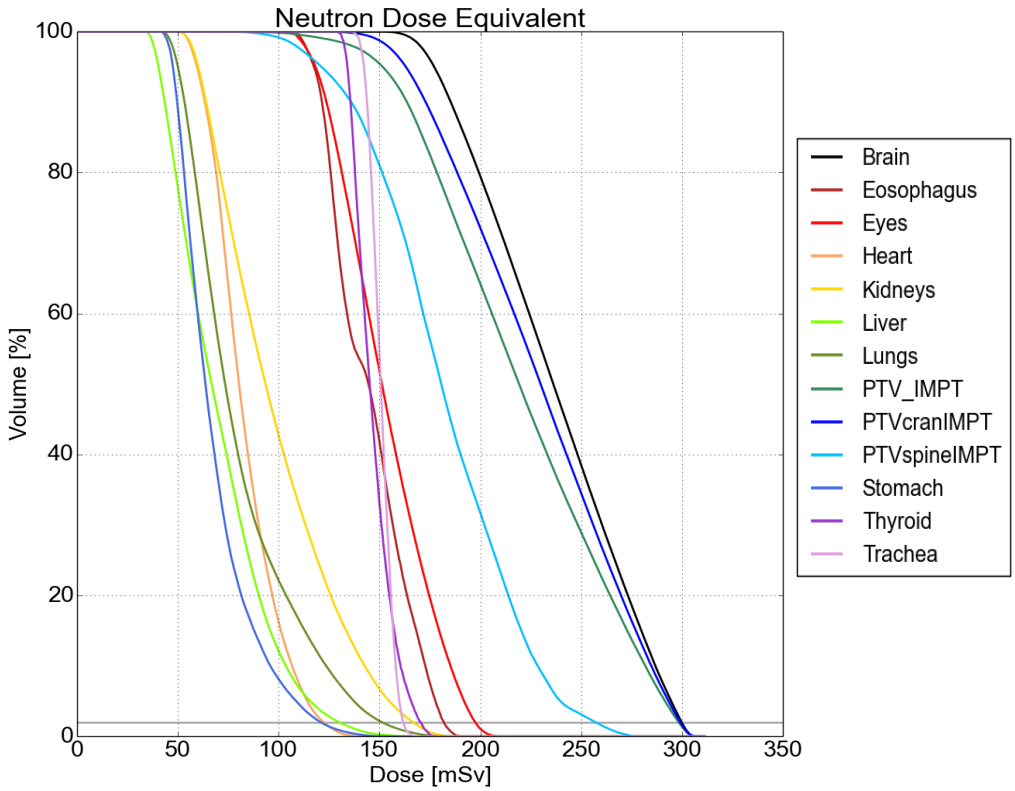

Figure 6.7: Dose equivalent DVH for selected organs. The lower organs lower in the patient body absorbed less neutron dose than the upper ones.

The first five lines in figure 6.7 are organs located in the lower parts of the body: stomach, liver, lungs and kidneys. They were the least exposed to neutron radiation. The trachea, esophagus, thyroid and spinal PTV were moderately exposed. The brain, cranial PTV and the total PTV received most stray radiation during the CSI treatment.

The same groups of lines were recognized in the neutron equivalent DVH (figure 6.7).

From the DVH, the following DVH metrics were obtained:

Table 6.1: DVH metrics of neutron absorbed dose values for chosen organs.

Structure	**Mean dose [mGy]**	D_{98} $[mGy]$	D_{50} $[mGy]$	D_2 $[mGy]$
Brain	4.4	3.1	4.4	5.7
Esophagus	1.8	1.2	1.8	2.7
Eyes	2.7	1.9	2.7	3.7
Heart	0.1	0.6	1.0	1.6
Kidneys	1.1	0.5	1.0	1.9
Liver	0.8	0.3	0.8	1.6
Lungs	1.0	0.5	0.9	2.0
PTV_IMPT	3.9	1.7	4.0	5.6
PTVcranIMPT	4.2	2.8	4.2	5.6
PTVspineIMPT	2.3	1.4	2.2	3.8
Stomach	0.8	0.4	0.7	1.6
Thyroid	2.0	1.5	2.0	2.5
Trachea	2.1	0.7	1.8	6.0

Table 6.2: DVH metrics of neutron dose equivalent values for chosen organs.

Structure	**Mean dose [mSv]**	D_{98} **[mSv]**	D_{50} **[mSv]**	D_2 **[mSv]**
Brain	236.0	170.1	236.2	299.8
Esophagus	144.6	113.2	144.5	181.9
Eyes	152.8	112.8	151.2	197.5
Heart	83.0	56.3	80.34	122.4
Kidneys	98.8	57.0	93.5	166.6
Liver	70.7	38.0	66.8	130.0
Lungs	81.2	47.3	73.4	151.3
PTV_IMPT	220.2	136.3	219.1	298.3
PTVcranIMPT	229.0	153.8	229.9	299.1
PTVspineIMPT	181.8	108.4	180.6	257.1
Stomach	68.6	45.6	63.7	120.9
Thyroid	146.7	132.5	145.1	170.4
Trachea	150.8	140.6	150.6	161.7

The brain was most exposed to neutron radiation of all organs; it received 4 mGy on average and the maximum and minimum doses were 5.7 mGy and 3.1 mGy respectively. It also absorbed most dose equivalent on average among all organs: 236 mSv, which was equal to the median dose it received. Considering the maximum dose the brain absorbed (300 mSv), 50% of the brain volume received a relatively homogenous dose between 230 and 300 mSv.

Following the brain, the organs that absorbed most doses on average were eyes, trachea and thyroid, with respective mean doses of 2.7 mGy, 2.1 mGy and 2.0 mGy respectively. Also the highest maximum and minimum doses were found in these organs. The highest D_2 was found in the trachea with 6 mGy, followed by the brain (5.7 mGy). Due to the high exposure of the brain, the minimum dose of this organ (3.1 mGy) exceeded the maximum doses of the lower organs, as these values ranged from 1-3 mGy.

The organs located lower in the body; stomach, liver, lungs, heart and kidneys, received mean neutron doses around 1 mGy. Their maximum doses were all in the order of 1-2 mGy, while the D_{98} was found to be in the range of 0.3 – 0.5 mGy.

The highest mean dose equivalents found in organs after the brain were again the eyes, trachea, thyroid and esophagus, all in the range of 140 - 155 mSv. The maximum doses were found to be the highest in the esophagus, thyroid, trachea and kidneys in the order of 160-180 mSv. Organs lower in the patient body received ~70 – 80 mSv, while the maximum and minimum doses for these organs were in the range of around 120-170 mSv and ~ 40 - 60 mSv respectively.

Considering the mean doses of all organs other than the brain, the D_{50} was found to be slightly closer to the D_{98} than the D_2 value. The difference between the median dose and D_2 was greater for lower organs than the upper ones.

Both PTVs received all the highest dose values among all irradiated structures, after the brain. Comparing the neutron-exposure in the spinal PTV with the cranial PTV; it seems evident that the cranial PTV absorbed more dose on average than the other target volume. All dose values in the absorbed neutron dose in the upper PTV was about twice as high as in the spinal PTV, except for the maximum dose.

The difference in dose values for the PTVs regarding the dose equivalent were around 40-50 mSv higher in the cranial PTV than in its spinal counterpart. As for the median dose, the D_{50} in the cranium was somewhat closer to the D_{98} than the D_2. The same applied to the spinal target volume.

7 Discussion

7.1 Neutron Dose Distributions

The data in figures 6.2 and 6.3 suggest that, due to the higher neutron doses in the head and neck, compared to the thorax and diaphragm, that more neutrons were produced in the upper body than in the lower part. This is in agreement with the fact that treatment volumes in the head were larger in volume compared to the spinal fields. Thus, more protons were needed for the cranial fields. Neutrons also seemed to penetrate deeper inside the patient in these areas. This comes from the beam configurations in the CSI treatment: two proton beams were aimed at the same target volume in the head, while the spinal beams each covered a part of the spine, with a small overlap. Since the cranial beams had energies ~ 40 MeV higher than the spinal beams, and the treatment fields were bigger than their spinal counterparts, as well as the cranial beams were aimed at the same PTV, these protons were able to produce more neutrons, as well as of higher energies. As the neutron interaction cross section decreases with increasing neutron energy, the mean free path becomes longer, increasing the penetration ability of the neutrons.

This ultimately resulted in higher dose distributions in the head and neck than in the thorax and diaphragm. The outermost regions in the lateral direction in the lower body parts were therefore in the order of 0.5 mGy, compared to the 2-3 mGy in the higher body.

This also explained the shape of the 1D plots in figure 6.4. As seen in figure 3.2, the neutron production cross section for protons were found to be at maximum for proton energies of $\sim$20 MeV. Due to the increasing number of neutrons produced, mainly with a forward directed distribution, we can observe an increase in neutron dose over the first few cm of the patient where the proton beams enter.

The peak in the 1D graphs occurred in three out of four heights in the patient body: head, throat and thorax, excluding the diaphragm. Because they occurred consistently after the PTV, it suggests that the positions of the peaks were dependent on the proton energies. Since doses were scored from neutrons only, this would indicate a correlation with the neutron production by protons.

However, as the 1D plots were volume-sensitive, they only give a feeling of the dose deposition inside the patient.

7.2 Neutron Doses in Organs

As seen in figure 6.2, the two cranial treatment fields with relatively high-energetic proton beams, lead to the highest exposure of organs to neutron radiation following the proton dose delivery. Because the target volume was inside the brain, this organ was by far the most exposed

of all organs. The fact that the median dose equivalent was so close to the maximum dose, implies that the brain was receiving quite homogeneous dose depositions in a large part of the volume, which was expected considering the dose delivery from the high-energy protons from the two cranial beams.

As seen from the metrics and figure 6.2, the upper organs were, after the brain, most exposed to stray radiation. They did however, absorb significantly less dose than the brain, since they were located outside the treatment fields. Secondary neutron doses are known to decrease rapidly with depth (Howell et al., 2016; Zacharatou Jarlskog et al., 2008)The dose equivalent of this exposure was, also after the brain, highest in this region, and lowest in the lower part of the body, as seen in figure 6.3. The median dose was also in overall closer to the maximum dose than in other structures.

As for the lower organs, they were not significantly exposed compared with the upper body. This is again due to the lower proton energies in this region and each field covering one part of the spine, as well as the smaller size of the treatment fields compared to the cranial ones. Since the median of the dose equivalents for these organs were close to the minimum dose, it suggests that neutron dose depositions within these structures were not as high as in the upper parts. This suggests that the risk of second malignancies from neutrons, such as radiation-induced cancer, could be lower in this part of the body.

Comparing the neutron doses both PTV's received, these data indicate that the area of the spinal PTV was less exposed to neutron radiation. Nevertheless, both PTVs were among the volumes that received the highest doses, both on average, maximum and minimum. This is expected as all proton beams were aimed at the respective target volumes.

Thus, neutron doses in overall were very small compared to the proton/total dose; it only accounted for around 0.02% of the total dose in the brain and in the order of 0.01% in the other organs. However, due to the large uncertainty in the carcinogenic potential of neutrons, i.e. the neutron RBE with respect to cancer induction, the neutron doses should be monitored and included in second cancer risk modeling.

The results were generally consistent with previous researches; Newhauser et al. (2005) simulated a CSI treatment for an adult male using IMPT and passively scattered proton therapy to compare the secondary dose distributions with the two delivery techniques (Newhauser et al., 2009). There were three differences between the study of Newhauser and this project: they used an adult male patient, the prescribed therapeutic dose was 36 Gy, and they scored neutron equivalent doses instead of ambient dose equivalent. The total doses received by OARs: thyroid, lungs, stomach, liver and esophagus received from stray radiation in the CSI treatment of Newhauser was calculated to compare the relative level of exposure in the organs with the results from the project. However, due to the differences in the treatment plan, and since they scored neutron equivalent dose instead of ambient dose equivalent, the data cannot be compared directly. The secondary neutron radiation scored by Newhauser et al. were similar with this

work; the thyroid and esophagus (upper organs) received the highest doses, followed by stomach, lungs and liver (lower organs).

The same trend was also found in a Monte Carlo study of CSI treatment using passively scattered proton therapy, performed by Taddei et al. in 2010 (Phillip et al., 2010). Although the female patient in their study was 4 years older and the therapeutic dose of 21.3 was slightly less, than the simulation used in this project, the upper organs: thyroid and esophagus, received more neutron dose than the lower organs: stomach, liver, and lungs.

This pattern was further emphasized by another study of Taddei et al. in 2009 in which the exposure to neutron radiation was evaluated for a wider selection of organs, including the brain (Taddei, Mirkovic, et al., 2009). The CSI treatment was delivered through passively scattered proton therapy, with a treatment dose of 30.6 to a ten year old boy. In their results: the level of exposure was the highest in the brain, followed by the eyes, thyroid and esophagus, and the lower organs. Ranking the organs after neutron exposure, the ranking was very similarly to the results in the thesis.

8 Conclusion

CSI treatment of a pediatric patient with medulloblastoma, using intensity-modulated proton therapy, lead to an unwanted secondary neutron dose distribution throughout the entire body of the patient. The data confirms that neutrons indeed scatter significantly, enlarging the lateral spread of the proton beam, as well as their strong penetration abilities. This enabled neutrons to reach targets far outside the well-defined treatment fields and deposit their dose in all organs that were considered in the body. Therefore, second malignancies could occur anywhere in the patient.

The neutron absorbed doses decreased gradually as one moves from the head towards the lower body parts. Therefore, the highest neutron absorbed- and dose equivalents were observed in the upper body, especially the brain. Because the cranial target volume was located in this organ, it received the highest neutron absorbed- and dose equivalents among all organs. The PTVs were as well among the volumes that received the highest absorbed- and dose equivalents.

The eyes, thyroid, trachea and esophagus received neutron absorbed- and dose equivalents in the order 2 mGy and 150 mSv. The stomach, kidneys, lungs and liver were also exposed, receiving considerable doses, in the order of 1 mGy and 80 mSv .

The organ specific neutron doses obtained in this work could be used as a data library for estimation of the risk of secondary cancer from neutron exposure during CSI treatment with protons. Such predictive modelling is essential for guiding radiation oncologist in choice of treatment for their patients.

Assessment of the risk of induced second malignancies due to neutron doses is recommended as further work. They can provide detailed information about the impact of IMPT by evaluating the potential risk of radiation damage in each organ individually. Using risk models with patient-specific parameters such as age and size is highly recommended.

Bibliography

A. Ferrari, P. R. S., A. Fasso, J. Ranft. Fluka: a multi-particle transport code. *Cern-2005-10 (2005), iNFN/TC_05/11, SLAC-R-773*.

ABTA. (2006). Focusing on Tumors: Medulloblastoma.

Agosteo, S., Birattari, C., Caravaggio, M., Silari, M., & Tosi, G. (1998). Secondary neutron and photon dose in proton therapy. *Radiother Oncol, 48*(3), 293-305.

Amaldi, U., & Kraft, G. (2005). Radiotherapy with beams of carbon ions. *Reports on Progress in Physics, 68*(8), 1861.

Baiocco, G., Alloni, D., Babini, G., Mariotti, L., & Ottolenghi, A. (2015). Reaction mechanism interplay in determining the biological effectiveness of neutrons as a function of energy. *Radiation protection dosimetry*, ncv134.

Baiocco, G., Barbieri, S., Babini, G., Morini, J., Alloni, D., Friedland, W., . . . Ottolenghi, A. (2016). The origin of neutron biological effectiveness as a function of energy. *Sci Rep, 6*, 34033. doi:10.1038/srep34033

Ballarini, F., Altieri, S., Bortolussi, S., Giroletti, E., & Protti, N. (2013). A model of radiation-induced cell killing: insights into mechanisms and applications for hadron therapy. *Radiat Res, 180*(3), 307-315. doi:10.1667/RR3285.1

Bauer, J., Sommerer, F., Mairani, A., Unholtz, D., Farook, R., Handrack, J., . . . Parodi, K. (2014). Integration and evaluation of automated Monte Carlo simulations in the clinical practice of scanned proton and carbon ion beam therapy. *Phys Med Biol, 59*(16), 4635-4659. doi:10.1088/0031-9155/59/16/4635

Bedogni, R. (2006). *Neutron spectrometry and dosimetry for radiation protection around a high energy electron/positron collider.* (Ph.D.), Universitat Autònoma de Barcelona.

Beiser, A. (2002). Concepts of Modern Physics (Sixth ed., pp. 441-443). New York: McGraw-Hill Europe.

Bethe, H. (1930). Zur Theorie des Durchgangs schneller Korpuskularstrahlen durch Materie. *Annalen der Physik, 397*(3), 325-400. doi:10.1002/andp.19303970303

Beyzadeoglu, M., Ozyigit, G., & Ebruli, C. (2010). Clinical Radiation Oncology *Basic Radiation Oncology* (pp. 145-173): Springer.

Bloch, F. (1933). Zur Bremsung rasch bewegter Teilchen beim Durchgang durch Materie. *Annalen der Physik, 408*(3), 285-320. doi:10.1002/andp.19334080303

Bragg, W. H., & Kleeman, R. (1904). LXXIV.On the ionization curves of radium. *Philosophical Magazine Series 6, 8*(48), 726-738. doi:10.1080/14786440409463246

Brenner, D. J., Elliston, C. D., Hall, E. J., & Paganetti, H. (2009). Reduction of the secondary neutron dose in passively scattered proton radiotherapy, using an optimized pre-collimator/collimator. *Phys Med Biol, 54*(20), 6065-6078. doi:10.1088/0031-9155/54/20/003

Brodin, N. P., Munck Af Rosenschold, P., Aznar, M. C., Kiil-Berthelsen, A., Vogelius, I. R., Nilsson, P., . . . Bjork-Eriksson, T. (2011). Radiobiological risk estimates of adverse events and secondary cancer for proton and photon radiation therapy of pediatric medulloblastoma. *Acta Oncol, 50*(6), 806-816. doi:10.3109/0284186X.2011.582514

Cameron, J. (1991). Radiation dosimetry. *Environmental Health Perspectives, 91*, 45-48.

Catli, S., & Tanir, G. (2013). Experimental and Monte Carlo evaluation of Eclipse treatment planning system for effects on dose distribution of the hip prostheses. *Med Dosim, 38*(3), 332-336. doi:10.1016/j.meddos.2013.03.005

Christóvão, M. T., & Campos, T. P. R. d. (2010). Análise da distribuição espacial de dose absorvida em próton terapia ocular. *Radiologia Brasileira, 43*, 249-254.
Commerce, N. U. D. o. NIST Stopping-Power and Range Tables: Electrons, Protons, Helium Ions.
Das, I. J., & Paganetti, H. (2015). *Principles and Practice of Proton Beam Therapy*: Medical Physics Pub Corp.
Durante, M., & Paganetti, H. (2016). Nuclear physics in particle therapy: a review. *Reports on Progress in Physics, 79*(9), 096702.
Engels, H., Menzel, H. G., Pihet, P., & Wambersie, A. (1999). Risk assessment for cancer induction after low- and high-LET therapeutic irradiation. *Strahlenther Onkol, 175 Suppl 2*(2), 47-51. doi:10.1007/bf03038888
Fano, U. (1963). Penetrations of protons, alpha particles, and mesons. *Annual Review of Nuclear Science, 13*, 1-66.
Ferrari, A., Sala, P. R., Fasso, A., & Ranft, J. (2014). *FLUKA: A multi-particle transport code (Manual)*. Retrieved from
Fjæra, L. F. (2016). *Development of a Monte Carlo Based Treatment Planning Verification Tool for Particle Therapy.* (Master), University of Bergen, Bergen.
Gottschalk, B. (2011). Physics of proton interactions in matter. *Proton Therapy Physics, Series in Medical Physics and Biomedical Engineering*, 19-60.
Grassberger, C., & Paganetti, H. (2011). Elevated LET components in clinical proton beams. *Phys Med Biol, 56*(20), 6677-6691. doi:10.1088/0031-9155/56/20/011
Grassberger, C., Trofimov, A., Lomax, A., & Paganetti, H. (2011). Variations in linear energy transfer within clinical proton therapy fields and the potential for biological treatment planning. *Int J Radiat Oncol Biol Phys, 80*(5), 1559-1566. doi:10.1016/j.ijrobp.2010.10.027
Grubbé, E. H. (1933). Priority in the Therapeutic Use of X-rays. *Radiology, 21*(2), 156-162. doi:10.1148/21.2.156
Grupen, C., & Shwartz, B. (2008). *Particle detectors* (Vol. 26): Cambridge university press.
Hajdu, S. I. (2011). A note from history: landmarks in history of cancer, part 1. *Cancer, 117*(5), 1097-1102. doi:10.1002/cncr.25553
Hale, G., M., & Hofmann, H., M. (2004). Neutron standard cross sections for 1H and 6Li from R-matrix analyses and microscopic calculations for the N-N and 7Li systems. Washington, D.C. :: United States. Dept. of Energy ;.
Hall, E. J., & Giaccia, A. J. (2006). *Radiobiology for the Radiologist*: Lippincott Williams & Wilkins.
Henley, E. M. G., Alejandro. (2007). Subatomic Physics (Third ed., pp. 40). Signapore: World Scientific Publishing Co. Pte. Ltd. (Reprinted from: 2010).
Hong, L., Goitein, M., Bucciolini, M., Comiskey, R., Gottschalk, B., Rosenthal, S., . . . Urie, M. (1996). A pencil beam algorithm for proton dose calculations. *Physics in Medicine and Biology, 41*(8), 1305.
Howell, R. M., Burgett, E. A., Isaacs, D., Price Hedrick, S. G., Reilly, M. P., Rankine, L. J., . . . Klein, E. E. (2016). Measured Neutron Spectra and Dose Equivalents From a Mevion Single-Room, Passively Scattered Proton System Used for Craniospinal Irradiation. *Int J Radiat Oncol Biol Phys, 95*(1), 249-257. doi:10.1016/j.ijrobp.2015.12.356
ICRP. (2007). The 2007 Recommendations of the International Commission on Radiological Protection. ICRP publication 103. *Ann ICRP, 37*(2-4), 1-332. doi:10.1016/j.icrp.2007.10.003
ICRP. (2011). Report 85. *Journal of the International Commission on Radiation Units and Measurements, 11*(1), NP-NP. doi:10.1093/jicru/ndr012

ICRU. (1993). *Quantities and units in radiation protection dosimetry*: International Commission on Radiation Units and Measurements.
ICRU. (2007). Prescribing, Recording, and Reporting Proton-Beam Therapy. *International Commission on Radiation Units and Measurements Report 78, Report No. 78*.
ICRU. (2011). Report 85: Fundamental quantities and units for ionizing radiation. *J icru, 11*(1), 1-31. doi:10.1093/jicru/ndr011
INFN. (2008). *Asimmetrie* (Vol. 21): Rivista dell'Istituto Nazionale di Fisica Nucleare.
Islam, M. R., Zheng, Y., Collums, T. L., Monson, J. M., Ahmad, S., & Benton, E. R. (2017). Measurement and simulation of secondary neutrons from uniform scanning proton beams in proton radiotherapy. *Radiation Measurements, 96*, 8-18. doi:http://dx.doi.org/10.1016/j.radmeas.2016.11.008
Jadrnickova, I., Spurny, F., & Molokanov, A. G. (2007). Contribution of secondary particles to the dose in 12C radiotherapy and other heavy ion beams. *Radiat Prot Dosimetry, 126*(1-4), 657-659. doi:10.1093/rpd/ncm133
Jarlskog, C. Z., & Paganetti, H. (2008). Sensitivity of different dose scoring methods on organ-specific neutron dose calculations in proton therapy. *Phys Med Biol, 53*(17), 4523-4532. doi:10.1088/0031-9155/53/17/004
Jermann, M. (2015). *Particle Therapy Patient Statistics*: PTCOG.
Jiang, H., & Paganetti, H. (2004). Adaptation of GEANT4 to Monte Carlo dose calculations based on CT data. *Med Phys, 31*(10), 2811-2818. doi:10.1118/1.1796952
Jiang, H., Wang, B., Xu, X. G., Suit, H. D., & Paganetti, H. (2005). Simulation of organ-specific patient effective dose due to secondary neutrons in proton radiation treatment. *Phys Med Biol, 50*(18), 4337-4353. doi:10.1088/0031-9155/50/18/007
Jones, B. (2015a). A Simpler Energy Transfer Efficiency Model to Predict Relative Biological Effect for Protons and Heavier Ions. *Front Oncol, 5*, 184. doi:10.3389/fonc.2015.00184
Jones, B. (2015b). Towards Achieving the Full Clinical Potential of Proton Therapy by Inclusion of LET and RBE Models. *Cancers (Basel), 7*(1), 460-480. doi:10.3390/cancers7010460
Juste, B., Miró, R., Campayo, J. M., Díez, S., & Verdú, G. (2010). Radiotherapy treatment planning based on Monte Carlo techniques. *Nuclear Instruments and Methods in Physics Research Section A: Accelerators, Spectrometers, Detectors and Associated Equipment, 619*(1), 252-257. doi:http://dx.doi.org/10.1016/j.nima.2009.10.127
Khan, F. M., & Gibbons, J. P. (2014). *Khan's the physics of radiation therapy*: Lippincott Williams & Wilkins.
Koning, A. J., & Rochman, D. (2012). Modern Nuclear Data Evaluation with the TALYS Code System. *Nuclear Data Sheets, 113*(12), 2841-2934. doi:http://dx.doi.org/10.1016/j.nds.2012.11.002
Kooy, H. M., & Grassberger, C. (2015). Intensity modulated proton therapy. *The British Journal of Radiology, 88*(1051), 20150195. doi:10.1259/bjr.20150195
Kroese, D. P., Brereton, T., Taimre, T., & Botev, Z. I. (2014). Why the Monte Carlo method is so important today. *Wiley Interdisciplinary Reviews: Computational Statistics, 6*(6), 386-392. doi:10.1002/wics.1314
Larsen, I. K. (2015). *Cancer in Norway 2014 - Cancer incidence, mortality, survival and prevalence in Norway (2015)* (I. K. Larsen Ed.). Oslo: Cancer Registry of Norway.
Lederman, M. (1981). The early history of radiotherapy: 1895–1939. *International Journal of Radiation Oncology*Biology*Physics, 7*(5), 639-648. doi:http://dx.doi.org/10.1016/0360-3016(81)90379-5
Leo, W. R. (1994). *Techniques for Nuclear and Particle Physics Experiments: A How-to Approach*: Springer.

Manem, V. S., Kohandel, M., Hodgson, D. C., Sharpe, M. B., & Sivaloganathan, S. (2015). The effect of radiation quality on the risks of second malignancies. *Int J Radiat Biol, 91*(3), 209-217. doi:10.3109/09553002.2014.980466

Meinhold, C. B. (1996). *One hundred years of x-rays and radioactivity. Radiation protection: then and now*. Austria: Berger.

NCRP. (1971). *NCRP Report*: U.S. Department of Commerce, National Bureau of Standards.

Newhauser, W. D., Fontenot, J. D., Mahajan, A., Kornguth, D., Stovall, M., Zheng, Y., . . . Woo, S. (2009). The risk of developing a second cancer after receiving craniospinal proton irradiation. *Phys Med Biol, 54*(8), 2277-2291. doi:10.1088/0031-9155/54/8/002

Newhauser, W. D., & Zhang, R. (2015). The physics of proton therapy. *Phys Med Biol, 60*(8), R155-209. doi:10.1088/0031-9155/60/8/R155

Odland, O. H. (2014). Status of Particle Therapy Statistics in 2014. *ENLIGHT Highlights*.

Packer, R. J., Zhou, T., Holmes, E., Vezina, G., & Gajjar, A. (2013). Survival and secondary tumors in children with medulloblastoma receiving radiotherapy and adjuvant chemotherapy: results of Children's Oncology Group trial A9961. *Neuro Oncol, 15*(1), 97-103. doi:10.1093/neuonc/nos267

Paganetti, H. (2002). Nuclear interactions in proton therapy: dose and relative biological effect distributions originating from primary and secondary particles. *Physics in Medicine and Biology, 47*(5), 747.

Paganetti, H. (2011). *Proton Therapy Physics* (1st ed.): CRC Press.

Paganetti, H. (2013). Protons *Monte Carlo Techniques in Radiation Therapy* (pp. 201-222): Taylor & Francis.

Paganetti, H. (2014). Relative biological effectiveness (RBE) values for proton beam therapy. Variations as a function of biological endpoint, dose, and linear energy transfer. *Phys Med Biol, 59*(22), R419-472. doi:10.1088/0031-9155/59/22/R419

Paganetti, H., Jiang, H., Parodi, K., Slopsema, R., & Engelsman, M. (2008). Clinical implementation of full Monte Carlo dose calculation in proton beam therapy. *Physics in Medicine and Biology, 53*(17), 4825.

Park, S. H., & Kang, J. O. (2011). Basics of particle therapy I: physics. *Radiation Oncology Journal, 29*(3), 135-146. doi:10.3857/roj.2011.29.3.135

Parodi, K., Ferrari, A., Sommerer, F., & Paganetti, H. (2007). Clinical CT-based calculations of dose and positron emitter distributions in proton therapy using the FLUKA Monte Carlo code. *Physics in Medicine and Biology, 52*(12), 3369.

Phillip, J. T., Anita, M., Dragan, M., Rui, Z., Annelise, G., David, K., . . . Wayne, D. N. (2010). Predicted risks of second malignant neoplasm incidence and mortality due to secondary neutrons in a girl and boy receiving proton craniospinal irradiation. *Physics in Medicine and Biology, 55*(23), 7067.

Pinter, C., Lasso, A., Wang, A., Jaffray, D., & Fichtinger, G. (2012). SlicerRT: radiation therapy research toolkit for 3D Slicer. *Med Phys, 39*(10), 6332-6338. doi:10.1118/1.4754659

Rinard, P. (1991). Neutron interactions with matter. *Passive Nondestructive Assay of Nuclear Materials*, 357-377.

Roddy, E., & Mueller, S. (2016). Late Effects of Treatment of Pediatric Central Nervous System Tumors. *J Child Neurol, 31*(2), 237-254. doi:10.1177/0883073815587944

Ruddon, R. W. (2007). *Cancer biology*: Oxford university press.

Röntgen, W. C. (1898). Ueber eine neue Art von Strahlen. *Annalen der Physik, 300*(1), 1-11. doi:10.1002/andp.18983000102

Saha, G. B. (2012). *Physics and radiobiology of nuclear medicine*: Springer Science & Business Media.

Salt, C., Lennox, A. J., Takagaki, M., Maguire, J. A., & Hosmane, N. S. (2004). Boron and gadolinium neutron capture therapy. *Russian Chemical Bulletin, 53*(9), 1871-1888. doi:10.1007/s11172-005-0045-6

Schaffner, B., & Pedroni, E. (1998). The precision of proton range calculations in proton radiotherapy treatment planning: experimental verification of the relation between CT-HU and proton stopping power. *Physics in Medicine and Biology, 43*(6), 1579.

Schinz, H. R. (1930). Gegenwärtige Methoden der Krebsbestrahlung und ihre Erfolge. II. Verteilte Dosis. *Strahlentherapie und Onkologie, 37*, 31-49.

Schneider, U., Agosteo, S., Pedroni, E., & Besserer, J. (2002). Secondary neutron dose during proton therapy using spot scanning. *Int J Radiat Oncol Biol Phys, 53*(1), 244-251.

Schneider, U., & Halg, R. (2015). The Impact of Neutrons in Clinical Proton Therapy. *Front Oncol, 5*, 235. doi:10.3389/fonc.2015.00235

Schneider, U., Lomax, A., Pemler, P., Besserer, J., Ross, D., Lombriser, N., & Kaser-Hotz, B. (2006). The impact of IMRT and proton radiotherapy on secondary cancer incidence. *Strahlenther Onkol, 182*(11), 647-652. doi:10.1007/s00066-006-1534-8

Schneider, W., Bortfeld, T., & Schlegel, W. (2000). Correlation between CT numbers and tissue parameters needed for Monte Carlo simulations of clinical dose distributions. *Physics in Medicine and Biology, 45*(2), 459.

Sengbusch, E., Perez-Andujar, A., DeLuca, P. M., Jr., & Mackie, T. R. (2009). Maximum proton kinetic energy and patient-generated neutron fluence considerations in proton beam arc delivery radiation therapy. *Med Phys, 36*(2), 364-372. doi:10.1118/1.3049787

Serway, R. A., & Jewett, J. W. (2013). *Physics for scientists and engineers with modern physics*: Nelson Education.

Smith, N. B., & Webb, A. (2010). *Introduction to medical imaging: physics, engineering and clinical applications*: Cambridge university press.

Stannard, C., Sauerwein, W., Maree, G., & Lecuona, K. (2013). Radiotherapy for ocular tumours. *Eye, 27*(2), 119-127.

Stokkevag, C. H., Engeseth, G. M., Ytre-Hauge, K. S., Rohrich, D., Odland, O. H., Muren, L. P., . . . Petersen, J. B. (2014). Estimated risk of radiation-induced cancer following paediatric cranio-spinal irradiation with electron, photon and proton therapy. *Acta Oncol, 53*(8), 1048-1057. doi:10.3109/0284186X.2014.928420

Stokkevåg, C. H. (2016). *Model-based predictions of secondary cancer and late effect risks following particle therapy*. (PhD), University of Bergen, Bergen.

Sweet, D. L. (1981). Contrary to Nature By Michael B. Shimkin. *Perspectives in Biology and Medicine, 24*(4), 672-673.

T.T. Böhlen, F. C., M.P.W. Chin, A. Fasso, A. Ferrari, P.G. Ortega, A. Mairani, P.R. Sala, G. Smirnov, V. Vlachoudis. (2014). The Fluka Code: Developments and Challenges for High Energy and Medical Applications. *Nuclear Data Sheets 120*, 211-214.

Taddei, P. J., Krishnan, S., Mirkovic, D., Yepes, P., & Newhauser, W. D. (2009). Effective Dose from Stray Radiation for a Patient Receiving Proton Therapy for Liver Cancer. *AIP Conf Proc, 1099*, 445-449. doi:10.1063/1.3120070

Taddei, P. J., Mirkovic, D., Fontenot, J. D., Giebeler, A., Zheng, Y., Kornguth, D., . . . Newhauser, W. D. (2009). Stray radiation dose and second cancer risk for a pediatric patient receiving craniospinal irradiation with proton beams. *Phys Med Biol, 54*(8), 2259-2275. doi:10.1088/0031-9155/54/8/001

Thariat, J., Hannoun-Levi, J. M., Sun Myint, A., Vuong, T., & Gerard, J. P. (2013). Past, present, and future of radiotherapy for the benefit of patients. *Nat Rev Clin Oncol, 10*(1), 52-60. doi:10.1038/nrclinonc.2012.203

Tourovsky, A., Lomax, A. J., Schneider, U., & Pedroni, E. (2005). Monte Carlo dose calculations for spot scanned proton therapy. *Phys Med Biol, 50*(5), 971-981. doi:10.1088/0031-9155/50/5/019

Villagrasa, C., Dos Santos, M., Bianco, D., Gruel, G., Barquinero, J. F., & Clairand, I. (2014). RBE-LET relationship for proton and alpha irradiations studied with a nanodosimetric approach. *Radiat Prot Dosimetry, 161*(1-4), 449-453. doi:10.1093/rpd/ncu047

Wang, X., Sahoo, N., Zhu, R. X., Zullo, J. R., & Gillin, M. T. (2010). Measurement of neutron dose equivalent and its dependence on beam configuration for a passive scattering proton delivery system. *Int J Radiat Oncol Biol Phys, 76*(5), 1563-1570. doi:10.1016/j.ijrobp.2009.07.1732

Wernli, C. (2004). *External dosimetry: operational quantities and their measurement.* Paper presented at the Proceedings of the 11th International Congress of the International Radiation Protection Association (IRPA).

Wilson, R. R. (1946). Radiological use of fast protons. *Radiology, 47*(5), 487-491. doi:10.1148/47.5.487

Yajnik, S. (2012). *Proton Beam Therapy: How Protons are Revolutionizing Cancer Treatment*: Springer New York.

Yang, C., Li, D. L. D., Wang, G. W. G., Lin, L. L. L., Tasch, A. F., & Banerjee, S. (2002, 22-27 Sept. 2002). *Quantum mechanical model of electronic stopping power for ions in a free electron gas.* Paper presented at the Ion Implantation Technology. 2002. Proceedings of the 14th International Conference on.

Zacharatou Jarlskog, C., Lee, C., Bolch, W. E., Xu, X. G., & Paganetti, H. (2008). Assessment of organ-specific neutron equivalent doses in proton therapy using computational whole-body age-dependent voxel phantoms. *Phys Med Biol, 53*(3), 693-717. doi:10.1088/0031-9155/53/3/012

Zacharatou Jarlskog, C., & Paganetti, H. (2008). Risk of developing second cancer from neutron dose in proton therapy as function of field characteristics, organ, and patient age. *Int J Radiat Oncol Biol Phys, 72*(1), 228-235. doi:10.1016/j.ijrobp.2008.04.069

Zheng, Y., Fontenot, J., Taddei, P., Mirkovic, D., & Newhauser, W. (2008). Monte Carlo simulations of neutron spectral fluence, radiation weighting factor and ambient dose equivalent for a passively scattered proton therapy unit. *Phys Med Biol, 53*(1), 187-201. doi:10.1088/0031-9155/53/1/013

Zheng, Y., Ramirez, E., Mascia, A., Ding, X., Okoth, B., Zeidan, O., . . . Keole, S. (2011). Commissioning of output factors for uniform scanning proton beams. *Med Phys, 38*(4), 2299-2306. doi:10.1118/1.3569581

Zirkle, R. E., Marchbank, D. F., & Kuck, K. D. (1952). Exponential and sigmoid survival curves resulting from alpha and X irradiation of aspergillus spores. *Journal of Cellular and Comparative Physiology, 39*(S1), 75-85. doi:10.1002/jcp.1030390408

Appendix A

Absorbed Dose

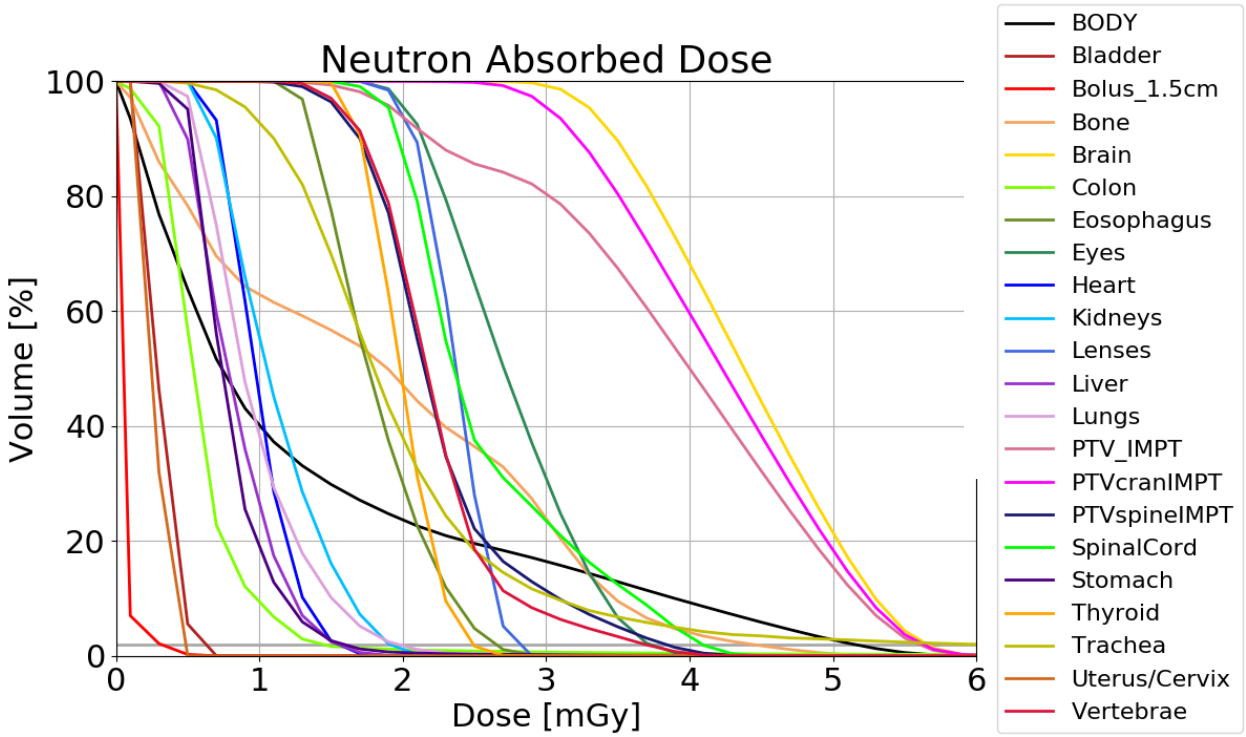

Figure A.1: Neutron absorbed dose DVH for all organs

Dose Equivalent

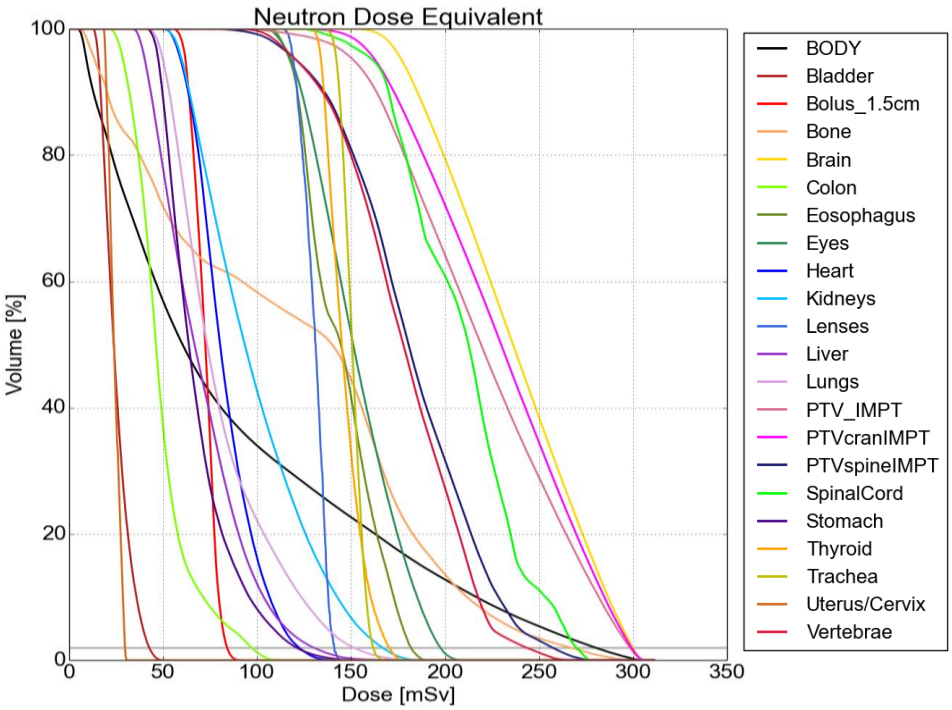

Figure A.2: Dose equivalent DVH for all organs

Appendix B

DVH metrics of all organs

Absorbed Dose

Table B.1: Absorbed dose for all organs

Structure	Mean dose [mGy]	D_{98} [mGy]	D_{50} [mGy]	D_{2} [mGy]
Bladder	0.3	0.1	0.3	0.6
Body	1.4	0.01	0.7	5.2
Bolus	0.01	0	0.1	0.3
Bone	1.8	0.1	1.9	4.4
Brain	4.4	3.1	4.4	5.7
Colon	0.6	0.1	0.5	1.5
Esophagus	1.8	1.2	1.8	2.7
Eyes	2.7	1.9	2.7	3.7
Heart	1.0	0.6	1.0	1.6
Kidneys	1.1	0.5	1.1	1.9
Lenses	2.4	1.9	2.4	2.8
Liver	0.8	0.3	0.8	1.6
Lungs	1.0	0.5	0.9	2.0
PTV_IMPT	3.9	1.7	4.0	5.6
PTVcranIMPT	4.2	2.8	4.2	5.6
PTVspineIMPT	2.3	1.4	2.2	3.8
SpinalCord	2.6	1.8	2.4	4.1
Stomach	0.8	0.4	0.74	1.6
Thyroid	2.0	1.5	2.0	2.5
Trachea	2.1	0.7	1.8	6.0
Uterus/Cervix	0.3	0.1	0.25	0.5
Vertebrae	2.2	1.4	2.2	3.7

Dose Equivalent

Table B.2: Dose equivalent values for all organs

Structure	Mean dose [mSv]	D_{98} [mSv]	D_{50} [mSv]	D_{2} [mSv]
Bladder	25.1	14.6	23.8	42.6
Body	89.7	7.5	60.4	279.9
Bolus	72.1	60.1	72.5	84.07
Bone	119.5	10.0	139.9	266.8
Brain	236.0	170.1	236.2	299.8
Colon	49.2	26.2	46.2	97.06
Esophagus	144.6	113.2	144.5	181.9
Eyes	152.8	112.8	151.2	197.5
Heart	83.0	56.3	80.3	122.4
Kidneys	98.8	56.9	93.4	166.6
Lenses	130.3	117.5	131.1	141.1
Liver	70.7	38.0	66.8	130.0
Lungs	81.2	47.3	73.4	151.3
PTV_IMPT	220.2	136.3	219.1	298.3
PTVcranIMPT	229.0	153.8	229.9	299.1
PTVspineIMPT	181.8	108.4	180.6	257.1
SpinalCord	209.0	146.8	212.5	269.9
Stomach	68.6	45.6	63.7	120.9
Thyroid	146.7	132.5	145.1	170.4
Trachea	150.8	140.6	150.6	161.7
Uterus/Cervix	24.2	19.0	23.9	29.7
Vertebrae	177.6	110.6	177.9	243.2

Appendix C

Neutron vs. therapeutic proton dose distribution from the CSI. Figures C.1 - C.4 a) show the neutron absorbed dose distribution, b) show the proton dose, c) show the neutron dose equivalent and d) show the location where the neutron dose was quantified.

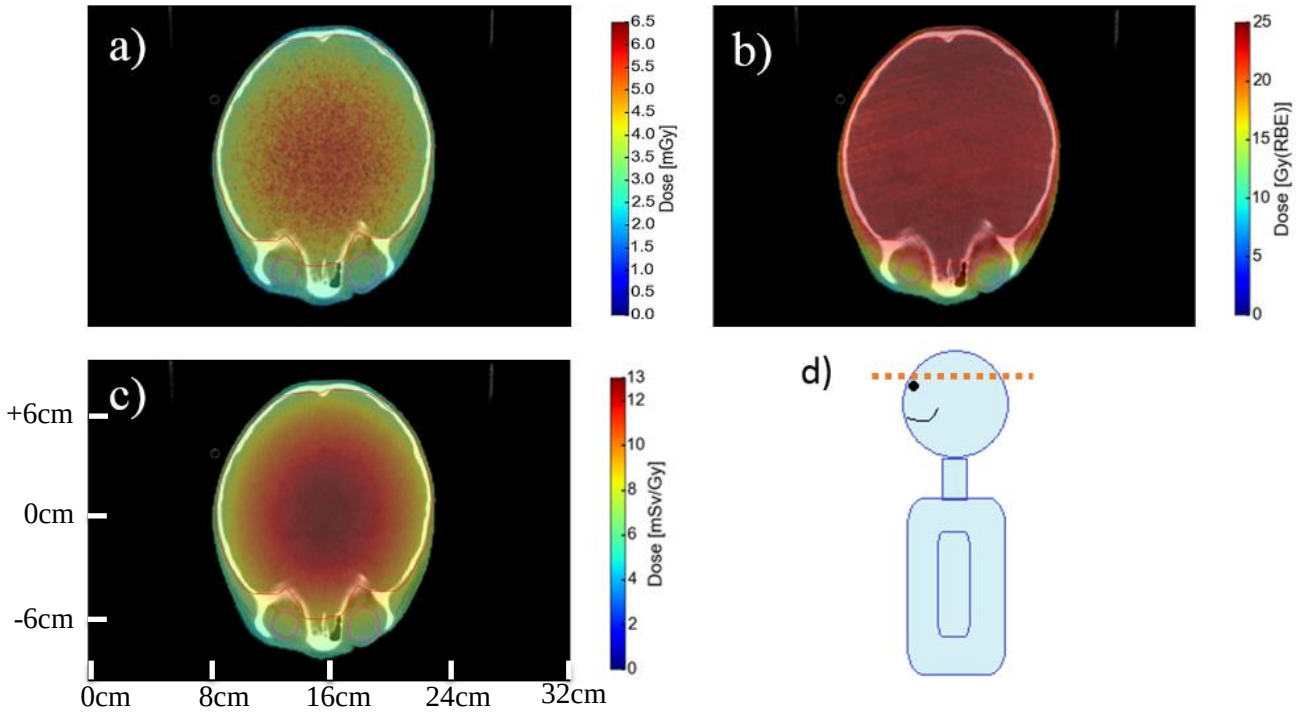

Figure C.1: Neutron vs proton quantified from the head in the patient

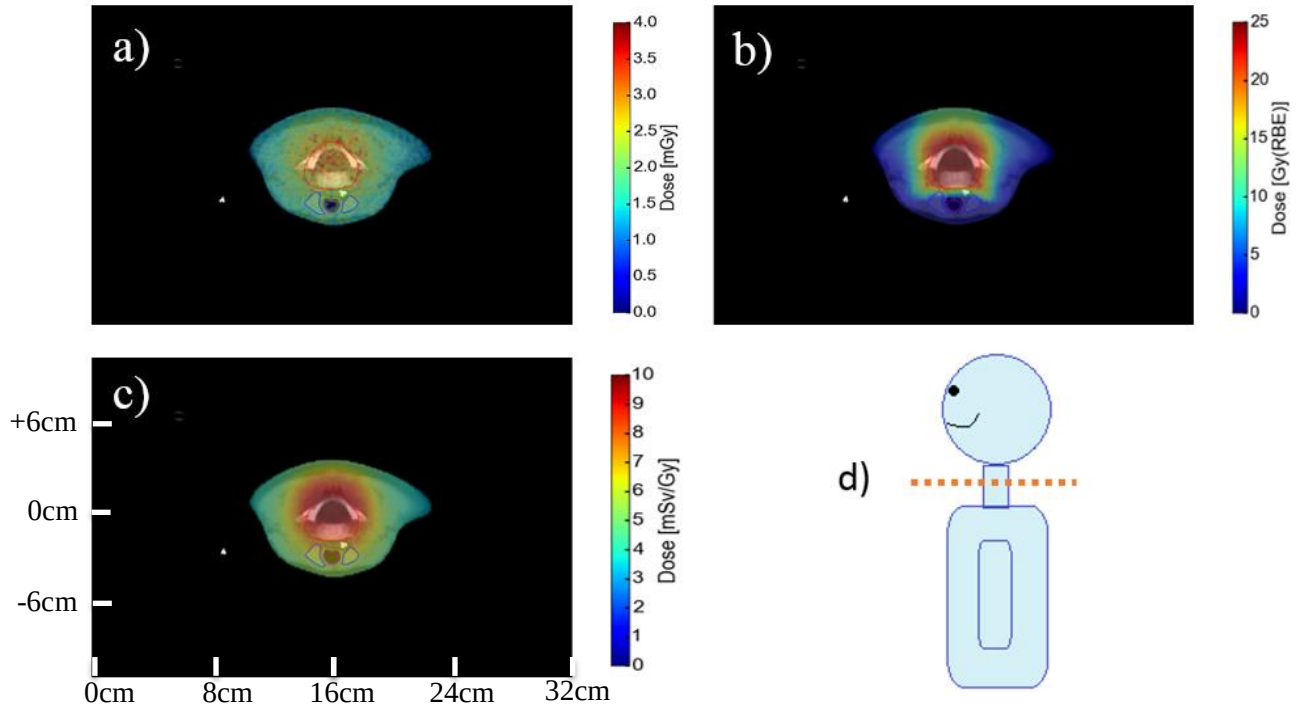

Figure C.2: Neutron vs proton quantified from the throat in the patient

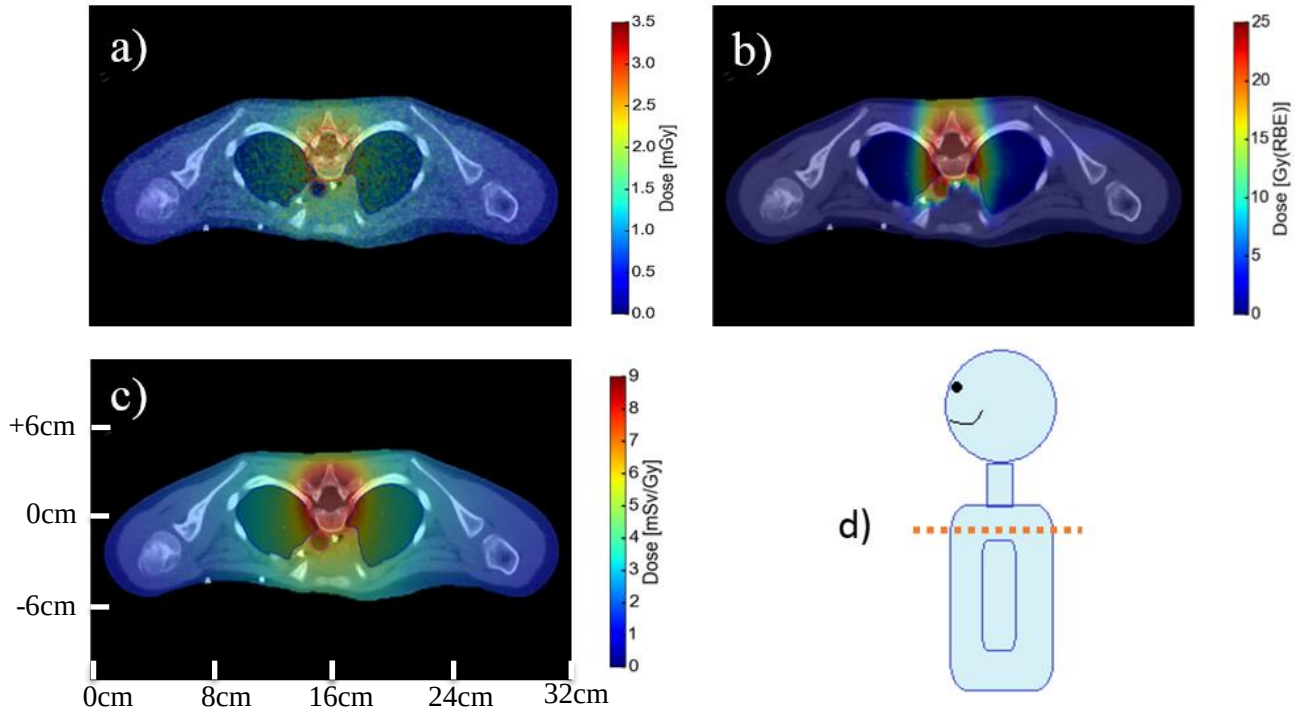

Figure C.3: Neutron vs proton quantified from the thoraxin the patient

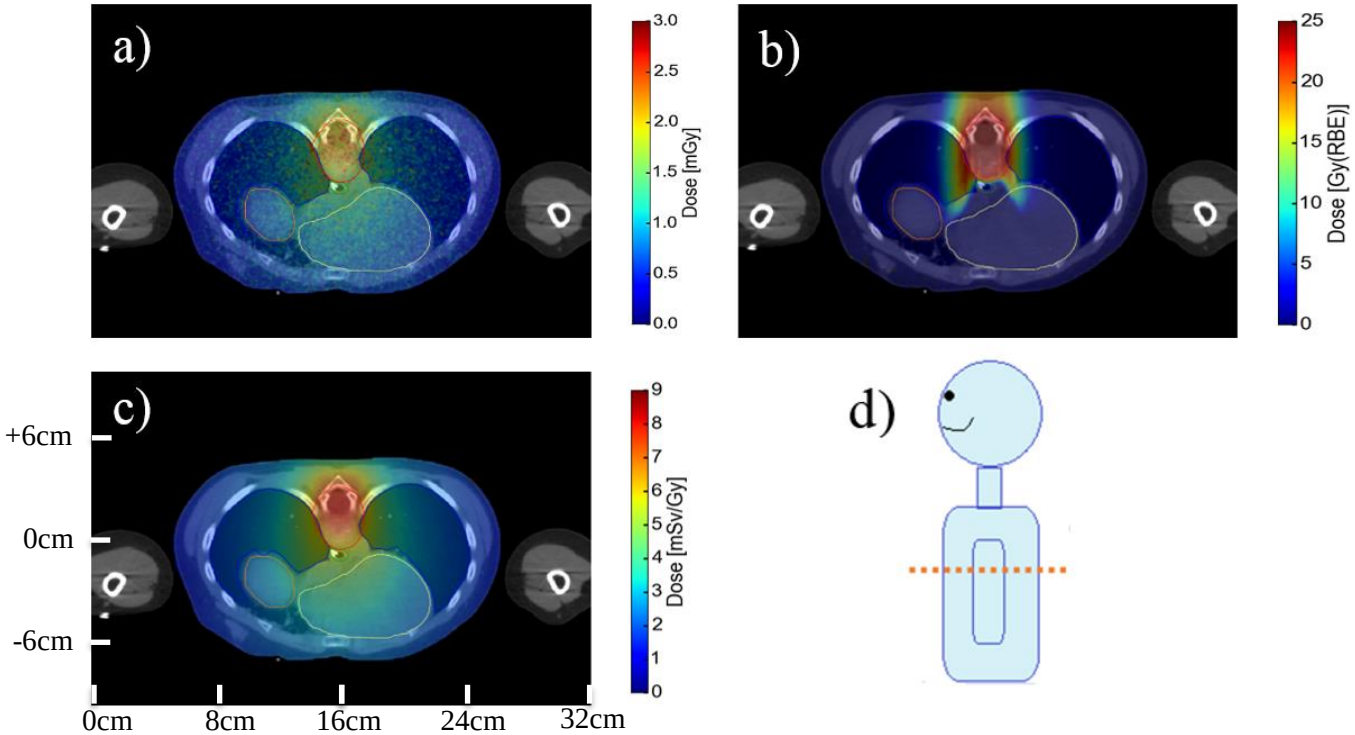

Figure C.4: Neutron vs proton quantified from the diaphragm in the patient